

Growth of Nanomaterials

17. Growth of Nanomaterials by Screw Dislocation

Fei Meng, Stephen A. Morin, Song Jin

Controlling the morphology of nanomaterials is important for their fundamental study and practical application. Especially one-dimensional nanowires, nanorods, and nanotubes and two-dimensional nanoplates possess interesting physical and chemical properties due to their structural anisotropy. The key to obtaining these morphologies is to break the symmetry of crystal growth to promote anisotropic growth. In this chapter we discuss the catalyst- and template-free screw-dislocation-driven nanomaterial growth mechanism, in which an axial screw dislocation creates self-perpetuating growth steps upon intersecting with the crystal surface and enables anisotropic crystal growth under low supersaturation conditions. The presence of screw dislocations not only alters the growth kinetics of nanomaterials, but also distorts the crystal lattice and generates a strain field, both of which lead to morphology variation of the nanomaterials. The structural characteristics associated with dislocation-driven growth can be readily detected using transmission electron microscopy techniques. A review is presented on a wide range of nanomaterials formed under various conditions whose growth has been confirmed to be driven by screw dislocations, demonstrating the generality of this mechanism. A framework for rationally synthesizing anisotropic nanomaterials via dislocation-driven growth is provided. This will enable large-scale, low-cost production of nanomaterials for various applications.

17.1	Classical Crystal Growth Theories	640
17.1.1	Layer-By-Layer Crystal Growth	640
17.1.2	Screw-Dislocation-Driven Crystal Growth	641
17.2	Theories for Screw-Dislocation-Driven Growth of Nanomaterials	642
17.2.1	Eshelby Twist	642
17.2.2	Dislocation-Driven Nanotube Formation	643
17.2.3	Dislocation-Driven Growth of 2-D Nanoplates	644
17.3	Structural Characterization of these Nanomaterials	645
17.3.1	Observation of Dislocation Contrast	645
17.3.2	Determination of Eshelby Twist	646
17.3.3	Lattice Tilt	648
17.3.4	Observation of Nanotubes or Voided NWS	649
17.4	Generality of Dislocation-Driven Nanomaterial Growth	649
17.4.1	Vapor-Phase Synthesis	650
17.4.2	Solution-Phase Synthesis	652
17.4.3	Solution Growth of 2-D Nanoplates	655
17.5	Rational Growth of Dislocation-Driven Nanomaterials – General Strategies	658
17.6	Applications	659
17.7	Summary and Perspectives	660
	References	661

One of the major goals in nanoscience and nanotechnology is to synthesize nanoscale building blocks of arbitrary dimensions, morphologies, and materials with increasing complexity from the bottom up. Anisotropic

nanomaterials have already found many applications and are therefore of great interest; For example, one-dimensional (1-D) nanowires (NWs), nanorods (NRs), and nanotubes (NTs) and two-dimensional

(2-D) nanoplates have shown new fundamental physical properties and demonstrated promising utility in nanoelectronics, nanophotonics, solar energy conversion, thermoelectricity, electrochemical energy storage, and chemical and biological sensing [17.1–9]. The fundamental understanding of the growth of anisotropic nanomaterials is critically important for developing rational and controllable synthesis to yield nanoscale morphologies suited for specific applications.

Several common mechanisms or methods have been established to explain bottom-up anisotropic NW growth or enable fabrication of 1-D nanomaterials. The vapor–liquid–solid (VLS) [17.10, 11] mechanism and other analogous catalyst-driven mechanisms, such as solution–liquid–solid (SLS) [17.12, 13] and vapor–solid–solid (VSS) [17.14] growth, have been the most commonly used methods for synthesis of NWs. In VLS (or SLS) growth, a nanoscale liquid droplet is formed between a nanoparticle metal catalyst and the desired precursor species due to eutectic phase behavior, and further supersaturation of the precursor leads to precipitation and growth of crystalline NW material from the catalyst. Use of 1-D templates such as anodic aluminum oxide (AAO) is another common way to confine the growth of nanomaterials to achieve 1-D growth [17.15]. The *oriented attachment* mechanism can also result in the formation of thin 1-D NWs in solution via the assembly of zero-dimensional (0-D) nanocrystals, as recently confirmed using the in situ transmission electron microscopy

(TEM) technique [17.16, 17]. From the perspective of crystal growth, the challenge of growing anisotropic nanomaterials, including 1-D NW materials, is to break the symmetry of crystal growth to ensure that crystals grow in a highly anisotropic fashion instead of forming bulk crystals with polyhedral shapes.

In this chapter, we discuss the screw-dislocation-driven mechanism for growth of anisotropic nanomaterials, in which axial screw dislocations provide self-perpetuating steps and break the symmetry of crystal growth. The key is to manipulate the kinetics of crystal growth and enable the formation of anisotropic crystals instead of polyhedral-shaped crystals or thin films [17.18–20]. The presence of the axial screw dislocations and the consequent strain field introduces unique characteristics to the dislocation-driven nanomaterial, including macroscopic growth kinetics and variations in nanostructure morphologies, which are explained next. We then introduce the technique to characterize these features in nanoobjects to confirm the growth mechanism. The generality of this mechanism is demonstrated by a survey of a wide range of different nanomaterials whose growth has been confirmed to be driven by screw dislocations. The general rule of design is then summarized to provide a framework for rationally synthesizing anisotropic nanomaterials via dislocation-driven growth, which may eventually enable large-scale, low-cost production of nanomaterials for various practical applications.

17.1 Classical Crystal Growth Theories

Since the key to successful anisotropic growth is controlling the kinetics of crystal growth and breaking the symmetry of crystal growth, we first review the fundamental kinetics of crystal growth processes [17.21].

17.1.1 Layer-By-Layer Crystal Growth

Layer-by-layer (LBL) crystal growth is the most intuitive mechanism for the formation of the extended periodic crystal structure of solids. However, due to the high energy barriers required to nucleate new layers of atoms which create step edges that facilitate the addition of more atoms (Fig. 17.1), LBL crystal growth theory predicts that much higher concentrations of gas-phase or liquid-phase precursors than the equilibrium con-

centration are necessary to enable a reasonable crystal growth rate. In other words, LBL growth requires high supersaturation. The supersaturation σ of the system is defined by (17.1) [17.21]

$$\sigma = \ln(c/c'), \quad (17.1)$$

where c is the precursor concentration and c' is the equilibrium concentration.

Study on the kinetics of LBL growth reveals that it has an *exponential* growth rate (R_{LBL}),

$$R_{\text{LBL}} = J_0 l^2 \beta \propto e^{(-g_n/kT)} l^2 \beta, \quad (17.2)$$

where J_0 is the rate of 2-D nucleation, l is the length of the facet (assuming a square growth facet), β is

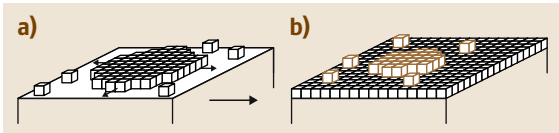


Fig. 17.1a,b Schematic illustration of the layer-by-layer crystal growth mechanism. (a) A 2-D island is nucleated and spreads to cover the active growth facet. (b) Once the first layer is completed, a new island (cluster of brown cubes) is nucleated on the first layer and the growth of a new layer begins

the step height, k is the Boltzmann constant, T is the temperature, and g_n is the energy barrier to 2-D nucleation, which is inversely proportional to supersaturation [17.21]. These expressions illustrate that LBL growth requires the formation of 2-D nuclei by overcoming the energy barrier g_n .

The prevailing catalyst-driven mechanisms, such as VLS [17.10, 11], SLS [17.12, 13], and VSS [17.14], that explain the 1-D anisotropic growth of NWs are fundamentally still LBL growth, but mediated by the catalyst droplets at the catalyst–solid interface [17.22, 23]. The nucleation barrier for LBL growth is lowered by the presence of the catalyst relative to the respective interface on the side-wall; therefore, the crystal growth is much faster at this interface. In this way, the symmetry of the crystal growth is broken and 1-D anisotropic crystal growth can proceed.

17.1.2 Screw-Dislocation-Driven Crystal Growth

Experimental observations reveal that crystal growth can actually happen under moderate supersaturation, contradicting the prediction of LBL growth theory. Frank [17.24, 25] solved this conflict by pointing out that crystals often have imperfections such as screw dislocation line defects [17.26, 27], which upon intersection with a crystal surface would make steps that propagate as spirals and thus become an endless source of crystal steps (Fig. 17.2). This theoretical model, known as the *Burton–Cabrera–Frank* (BCF) theory [17.24], successfully explains the observed growth rates of crystals under moderate and low supersaturation. Such surface dislocation spirals have been observed in many materials [17.28], and the dislocation-driven growth mechanism has become a cornerstone of crystal growth theory.

BCF theory predicts a dislocation growth rate ($R_{\text{dislocation}}$) that is linearly dependent on super-

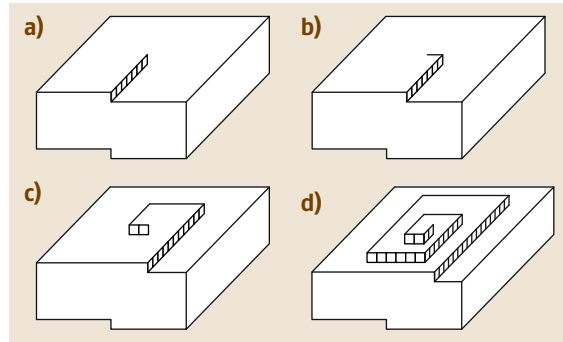


Fig. 17.2a–d Illustration of screw dislocation growth spirals. (a–d) Schematic illustration of a screw dislocation spiral propagating new step edges as the crystal grows (after [17.21])

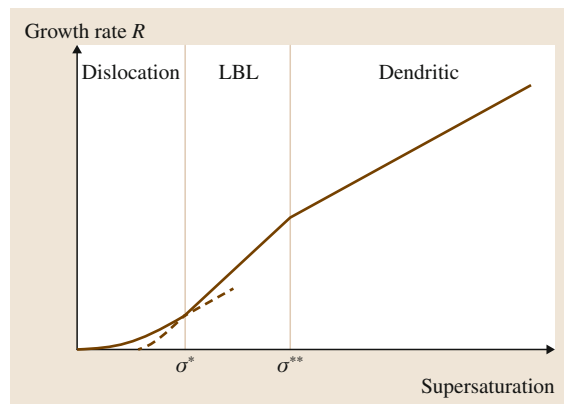


Fig. 17.3 Schematic illustration of crystal growth mechanism as a function of supersaturation. As the supersaturation increases, the dislocation, LBL, and dendritic growth mechanisms progressively dominate (after [17.20])

saturation

$$R_{\text{dislocation}} = C\sigma, \quad (17.3)$$

where C is a rate constant that depends on the maximum possible flux of monomers to the crystal surface via diffusion through the stagnant layer. This growth kinetics of the dislocation-driven mechanism is a characteristic feature that can distinguish it from other growth modes.

According to classical crystal growth theory, the growth mechanism of a crystal depends on the supersaturation. As schematically illustrated in Fig. 17.3, at low supersaturation the dislocation-driven spiral growth mechanism is followed; at intermediate supersaturation the LBL growth mechanism is followed; at high supersaturation the dendritic growth mechanism is followed.

These different growth regimes are separated by two characteristic supersaturations, namely σ^* and σ^{**} , at which the growth rate of the next mechanism overtakes the previous one (Fig. 17.3). In the context of current studies which focus on well-faceted single-crystalline nanomaterials, the dislocation growth and LBL growth mechanisms are the most relevant and are the topics of the following discussion.

17.2 Theories for Screw-Dislocation-Driven Growth of Nanomaterials

Screw dislocation has been proven to be responsible for both 1-D and 2-D crystal growth. The essence of screw-dislocation-driven nanomaterial growth, especially nanowire growth, is that, under appropriate low supersaturation conditions that favor dislocation-driven growth over LBL growth, crystal growth occurs more rapidly at the dislocation spirals along the axial direction whereas radial dimension expansion via the LBL mode is prohibited (Fig. 17.4a). In this way, the symmetry of the crystal growth is broken and highly anisotropic crystal growth is enabled by the self-perpetuating steps of screw dislocations.

The basic idea that screw dislocations can drive anisotropic growth of 1-D crystals was in fact proposed and discussed in the 1950s by Sears [17.29–32]. Indirect evidence such as lattice twist within whiskers was observed, suggesting the presence of axial screw dislocations [17.33, 34]. Decoration of axial dislocations in whiskers of alkali halides was first observed in 1958 [17.35]. Direct observation and identification

of screw dislocations in whiskers using electron microscopy was not reported until 1965, in single-crystal whiskers of aluminum nitride [17.36, 37], and later chalcotrichite (Cu_2O) [17.38]. In the modern literature, observation and confirmation of dislocation-driven NW growth was first reported in NW trees of PbS [17.18, 39] and PbSe [17.40]. In these fascinating tree-like structures, growth of the trunk is driven by screw dislocations whereas the branches are grown by the more traditional VLS NW growth mechanism.

17.2.1 Eshelby Twist

A screw dislocation disrupts the perfect periodicity within the crystal lattice and thereby causes a strain energy per unit length E that is quadratically dependent on the magnitude of the dislocation Burgers vector b , i. e.,

$$E = \frac{b^2 \mu}{4\pi} \int_{r_0}^R \frac{dr}{r} = \frac{b^2 \mu}{4\pi} \ln \left(\frac{R}{r_0} \right), \quad (17.4)$$

where μ is the shear modulus, R is the radius of the cylinder containing the dislocation, and r is the core radius of the dislocation. This stress field exerts a torque at the free ends of the rod, resulting in a twist of the rod along the axial direction (Fig. 17.4b) [17.26, 41], known as the Eshelby twist, which in turn serves as evidence of the dislocation-driven growth mechanism. This Eshelby twist is mathematically expressed as

$$\alpha = \frac{b}{\pi R^2}, \quad (17.5)$$

where α is the twist of the lattice in radians per unit length. Attempts to observe the Eshelby twist in micrometer-scale whiskers were made in the late 1950s, but the results were often inconclusive [17.34, 42]. Because of the $1/R^2$ dependence, the Eshelby twist is

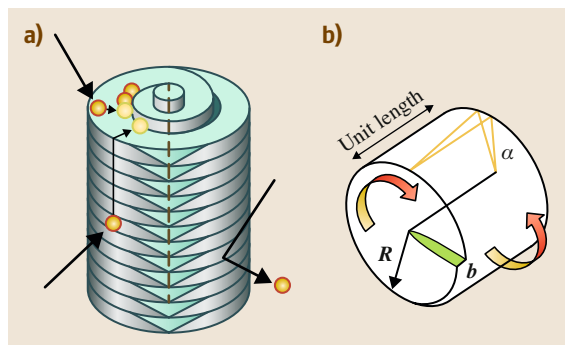


Fig. 17.4a,b Illustrations of screw-dislocation-driven NW growth and the associated Eshelby twist. (a) A screw dislocation drives 1-D growth at low supersaturation, where LBL growth is prohibited (after [17.19]); (b) Eshelby twist (after [17.18])

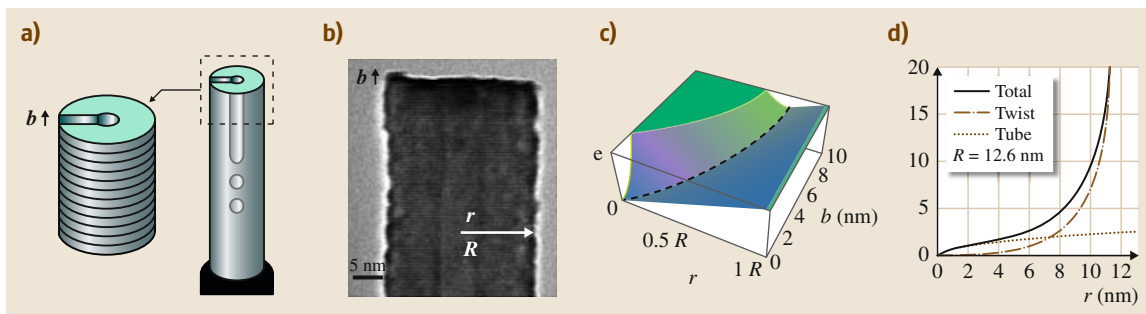


Fig. 17.5a–d Two pathways to relieve the strain energy and the estimation of b in ZnO NTs: **(a)** Schematic illustration of screw-dislocation-driven formation of a hollow NT. **(b)** High-resolution transmission electron microscopy (HRTEM) image of the tip of a ZnO NT in which the critical parameters R , r , and b can be directly measured. **(c)** Calculated three-dimensional (3-D) energy plot using (17.8) for the ZnO NT shown in **(b)**; the dashed line represents the energy minimum. **(d)** Energy-minimized relation for b versus r/R by explicitly solving (17.8) along this energy valley for the specific ZnO NT in **(b)**; the total contribution to b has components due to the hollow inner tube surface energy (red dash-dotted line) and to the Eshelby twist (blue dotted line) (after [17.20])

more pronounced at the nanoscale compared with in micrometer-sized whiskers, making it readily observable in NWs and NTs. Particularly in the case of hyperbranched nanostructures such as PbS and PbSe nanotrees, overgrowth of epitaxial branching nanowires allows easy visualization of the twist [17.18, 39, 40]. This allows direct measurement of the Eshelby twist and a simple estimate of the Burgers vector's screw component magnitude. In recent years, more accurate theoretical calculations of Eshelby twists based on molecular dynamics have been carried out for thin NW and NT materials [17.43, 44].

17.2.2 Dislocation-Driven Nanotube Formation

The formation of single-crystal NTs is a signature of nanomaterial growth driven by dislocations with large Burgers vector b (Fig. 17.5a). In the case of a hollow tube, the elastic energy caused by the dislocation can be expressed by modifying (17.4) as

$$E = \frac{b^2 \mu}{4\pi} \ln \left(\frac{R}{r} \right), \quad (17.6)$$

where R and r are the outer and inner tube radii, respectively [17.27]. As b increases, eventually the crystal contains enough strain energy that it exceeds the energy cost of creating a new inner surface and the dislocation core becomes hollow. This causes the formation of micropipes, which are often observed in dislocation-prone materials such as SiC or GaN and sometimes termed *open-core dislocations* [17.45, 46]. In the clas-

sical open-core dislocation model, an energy balance between the surface energy ($2\pi\gamma r$, where γ is the surface energy) and the strain energy from (17.6) (both per unit length) results in a relationship between r and b [17.45]

$$b_{\text{tube}} = \sqrt{\frac{8\pi^2 \gamma r}{\mu}}. \quad (17.7)$$

For NWs reaching this energy threshold, the solid NW becomes a hollow NT. In other words, the equilibrium morphology of 1-D nanomaterials whose growth is driven by screw dislocations should be hollow NTs when the Burgers vector is sufficiently large [17.47]. The commonly observed voided NWs [17.47, 48] might be an intermediate stage lying on the threshold, oscillating between the solid and hollow conditions due to small fluctuations in growth environment and NW thickness that subtly change the energy balance, or tubes initially formed could partially close up after synthesis.

Furthermore, forming a hollow core and producing a torque around the NW axis via the Eshelby twist mechanism are two competing pathways to alleviate the strain caused by the screw dislocations. Once the nanostructure becomes hollow, the overall energy per unit length E contains three terms: the surface energy of the hollow inner tube, the lattice strain due to the dislocation, and the reduction in lattice strain due to the Eshelby twist

$$E = 2\pi\gamma r + \frac{\mu b^2}{4\pi} \ln \left(\frac{R}{r} \right) - \frac{\mu b^2}{4\pi} \frac{(R^2 - r^2)}{(R^2 + r^2)}. \quad (17.8)$$

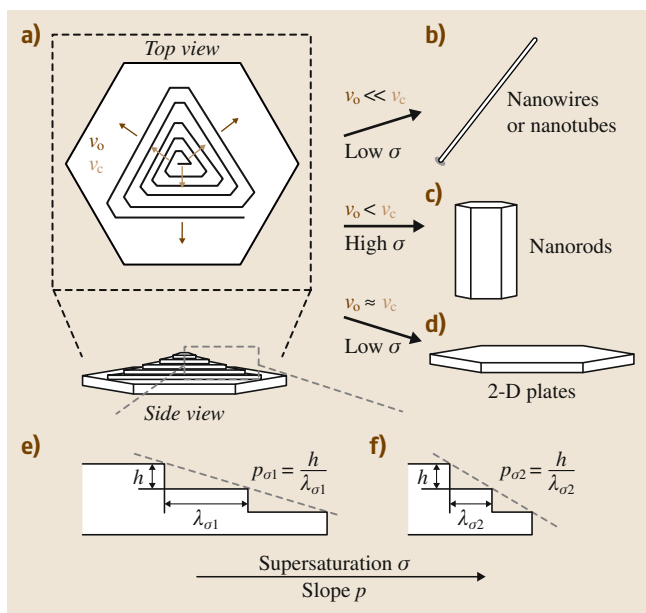


Fig. 17.6a–f A unified scheme illustrating dislocation-driven growth of various nanomaterial morphologies. (a) Top view and dramatized side view of an idealized nanoplate with one screw dislocation with various step velocities at the dislocation core (v_c) and the outer edges (v_o). Nanowires or nanotubes (b), nanorods (c), or nanoplates (d) are achieved when specific step velocity and supersaturation conditions are met. (e, f) Side views reveal the relationship between the nanoplate slope p , step height h , terrace width d , and supersaturation σ (after [17.50]) ◀

be alternately displayed as a plot of b versus r/R (Fig. 17.5d). It is clear from Fig. 17.5d that, when r/R is small, representing the scenario of a thick-walled NT, the total energy minimization approximates the Frank's open-core dislocation model, and most energy is relieved by making the tube hollow; however, at much larger r/R values, the total energy minimization begins to follow the Eshelby twist line, indicating that a thin-walled NT has more significant twist, as creating more surface becomes energetically unfavorable.

When ZnO nanotubes are used as a model system to evaluate (17.8), with the specific values of surface energy of 0.31 J/m^2 and shear modulus of 44.3 GPa [17.49], and the radii of the NT shown in Fig. 17.5b, a three-dimensional surface plot of (17.8) constructed for E versus b and r/R (Fig. 17.5b) shows that there is an energy valley (minimum) associated with certain optimized r and b values (marked with a dashed line). The energy-minimized relation between r and b can be solved by setting the energy derivative with respect to r to zero,

$$\frac{dE}{dr} = 0 \rightarrow b_{\text{total}} = \sqrt{\frac{8\pi^2\gamma r}{\mu}} \left(\frac{R^2 + r^2}{R^2 - r^2} \right). \quad (17.9)$$

The first factor in (17.9) represents the effect from Frank's open-core dislocation model in (17.7) [17.45], while the second factor is the modification due to the Eshelby twist pathway. The Eshelby twist component can also be expressed explicitly as the difference between (17.7) and (17.9),

$$b_{\text{twist}} = b_{\text{total}} - b_{\text{tube}} = \sqrt{\frac{8\pi^2\gamma r}{\mu}} \left(\frac{R^2 + r^2}{R^2 - r^2} - 1 \right). \quad (17.10)$$

This direct relation between the r and b variables along the energy valley (17.9; dashed line in Fig. 17.5c) contains the contributions to the total energy from the Eshelby twist and hollow tube components and can

17.2.3 Dislocation-Driven Growth of 2-D Nanoplates

Screw dislocations can also drive 2-D anisotropic crystal growth. The key herein is to control the crystal growth step velocities at different positions from the dislocation core (Fig. 17.6a) [17.51]. In general, the velocity of steps at the core v_c should be the same as those at the outer edges of the dislocation hillocks v_o due to their crystallographic equivalence. However, the velocity of steps can be affected by environmental factors such as impurities or mass transport, such that steps created earlier in growth (thus at the outer edge v_o) develop more slowly than newly generated steps closer to the core of the dislocation (v_c), which leads to two scenarios. When v_o is slightly less than v_c , newly generated steps from the dislocation core would very slowly catch up with those at the outer edge to create a step pile-up and thus a step-free facet, which will lead to low-aspect-ratio NRs or bulk polyhedral crystals (Fig. 17.6c), particularly when under higher supersaturation and if there is significant LBL growth. Furthermore, if v_o is much less than v_c , possibly because the steps at the outer edge have more impurity pinning sites, more adsorbed surfactants [17.52], or slower mass transport kinetics [17.7], newly generated steps quickly catch up with those further out, rapidly producing a step-free facet and thus leading to almost pure 1-D growth under low supersaturation conditions

(Fig. 17.6b). Finally, if v_0 is equal to v_c , which is more common in general crystal growth, all steps, regardless of whether they are newly generated steps at the dislocation core or earlier steps at the outer edge of the growth spiral, propagate at the same velocity and a step pile-up is never created; thus, the steps spread in 2-D (Fig. 17.6d).

According to BCF theory [17.51, 53], the terrace width d is inversely proportional to the supersaturation σ of the system, and thus, for the same step height h , the slope of the nanoplate hillocks ($p = h/d$) increases as the supersaturation increases (Fig. 17.6e,f). Therefore, the thickness-to-diameter ratio of 2-D nanoplates depends on the supersaturation of

the growth solutions; i. e., low-supersaturation growth favors generation of very thin nanoplates with small slopes, while higher supersaturation leads to thicker plates of increasing slope. This relationship between terrace width (and thus the slope of dislocation hillocks) and supersaturation has been well documented in crystal growth studies, such as those shown by *De Yoreo* et al. [17.52].

Despite the drastic difference between the morphologies of NWs, NTs, and nanoplates, their growth can be unified using the dislocation-driven mechanism. Understanding how to control the nanomaterial anisotropy is of great importance to design dislocation-driven growth for specific applications.

17.3 Structural Characterization of these Nanomaterials

Dislocation-driven growth is a general mechanism, and therefore the principles described above are applicable to many crystalline materials grown from solution or vapor phase. However, dislocations are mobile and especially not stable in small volumes [17.26, 27], so that postgrowth mechanical perturbation could work the dislocations out of nanomaterials. As a result, dislocations themselves might not always be directly visualized, and the operation of the dislocation-driven mechanism might have been overlooked in many anisotropic nanomaterials (especially 1-D nanomaterials) whose growth is not completely or correctly understood. Nevertheless, there is other evidence closely associated with the dislocation-driven growth mechanism that can support this mechanism, including the lattice twist, lattice tilt, and formation of hollow tubes. In this section we discuss the common techniques that can be used to characterize dislocation-driven nanomaterials.

17.3.1 Observation of Dislocation Contrast

Transmission electron microscopy (TEM) has been the most common and powerful tool used to analyze the microstructures of materials. Screw dislocations can be readily detected and their associated Burgers vectors identified using the diffraction-contrast TEM technique, which relies on additional electron diffraction due to the bending of atomic planes near the dislocation core. If an image is reconstructed from specific reciprocal-space diffraction spots \mathbf{g} that are selected by a physical aperture, these additional diffracted electrons create a visible contrast around the dislocation. However, diffraction

spots \mathbf{g} that are normal to the Burgers vector of the dislocation \mathbf{b} ($\mathbf{g} \times \mathbf{b} = 0$) produce no dislocation contrast – the *invisibility criterion* [17.54]. Therefore, the direction of a Burgers vector can be identified by taking the cross-product of two non-collinear \mathbf{g} vectors that make the dislocation contrast disappear. A general procedure for identifying the Burgers vector's direction is detailed in the following:

- First step: Tilt the sample onto an appropriate zone axis which contains the diffraction spots that are perpendicular to the potential Burgers vector's direction. Most crystal lattice types have their own habitual Burgers vectors, for example, [110] in the face-centered cubic (fcc) structure or [001] in the hexagonal closed-packed (hcp) structure [17.26]. Otherwise, the growth direction of NWs can be well used as a guide to screen the \mathbf{g} vectors and the corresponding zone axes, because the axial growth direction by definition has to be parallel to the screw component of the dislocation Burgers vector that is responsible for driving the NW growth.
- Second step: Approach the two-beam condition by further tilting the sample until almost all other reflections disappear with the exception of the transmitted beam (the zero beam) and the selected \mathbf{g} beam. Repeat these two steps to find another non-collinear \mathbf{g} beam that satisfies the invisibility criterion.
- Third step: Determine the Burgers vector direction by taking the cross-product of the \mathbf{g} vectors. Ap-

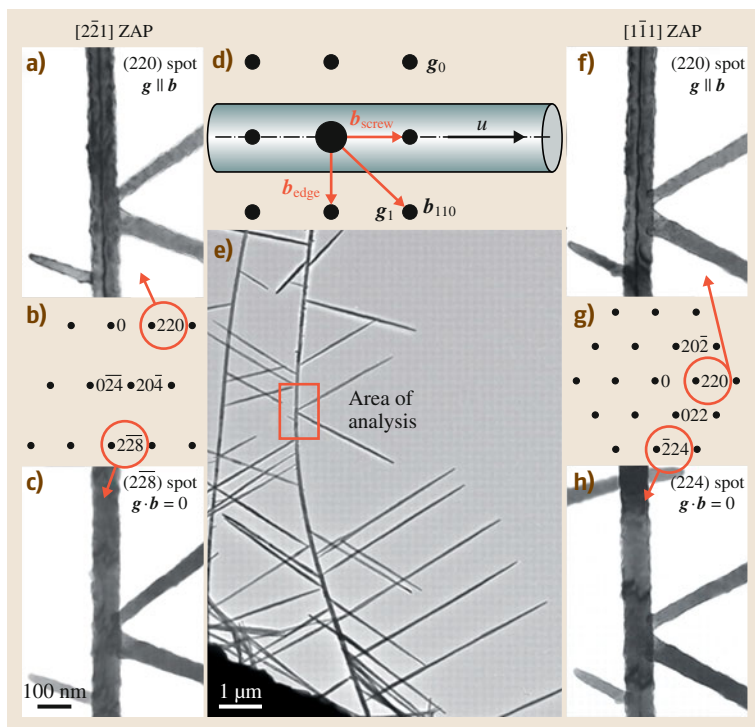


Fig. 17.7a–h Diffraction-contrast TEM imaging of the dislocation in the tree trunk: (a–c) TEM images along the $[2\bar{2}1]$ zone axis under strong two-beam conditions; (a) $g\parallel b$ conditions showing strong diffraction contrast; (c) invisibility conditions as highlighted (red circles) in the zone axis diagram (b). (a) Schematic superposition of real and reciprocal space of a dislocation-containing NW along the $[001]$ zone axis is shown to illustrate the Burgers vector relationship. (b) Low-magnification TEM image showing the tree and area analyzed. (c–e) $[1\bar{1}1]$ zone axis TEM under strong two-beam conditions. (f) $g\parallel b$ conditions and (h) invisibility conditions as highlighted (red circles) in the zone axis diagram (g) (ZAP: zone axis pattern; after [17.18])

proach the two-beam condition composed of the zero beam and the determined Burgers vector beam to verify the presence of strong dislocation contrast (the $g\parallel b$ condition that exhibits the highest contrast of dislocations).

The determination of the Burgers vector in the PbS tree-like structure can be used as an example to illustrate the entire process [17.18]. The same segment of a tree structure was tilted to the $[2\bar{2}1]$ zone axis (Fig. 17.7a–c) and the $[1\bar{1}1]$ zone axis (Fig. 17.7f–h), respectively. The dislocation meets the invisibility criterion under the perpendicular $(2\bar{2}\bar{8})$ two-beam condition near the $[2\bar{2}1]$ zone axis and the perpendicular $(\bar{2}24)$ two-beam condition near the $[1\bar{1}1]$ zone axis. Therefore, taking the cross-product of the $(2\bar{2}\bar{8})$ and $(\bar{2}24)$ vectors shows that the Burgers vector is along the $[110]$ direction, which is confirmed by the images under two-beam conditions of the parallel $[220]$ spots showing high contrast of the dislocation line. It is known that the Burgers vector of the most stable dislocations in rock-salt crystals is along $\langle 110 \rangle$, and this has been previously observed in bulk PbS crystals [17.26, 55]. Since the dislocation line direction (u) is along the $[100]$ NW growth direction, the $[110]$ Burgers vec-

tor represents a mixed dislocation: a screw dislocation component along the $[100]$ (or $[\bar{1}00]$) direction mostly responsible for driving the NW growth, and an edge dislocation component along the $[010]$ (or $[0\bar{1}0]$) direction. The role of edge dislocations in promoting crystal growth [17.56] is not clear but cannot be ruled out completely at present.

Using such methods, dislocation contrast has been conclusively observed for NWs of PbS [17.18, 39], PbSe [17.40], CdS, CdSe [17.57], AlN [17.37], ZnO [17.20, 47], α -FeOOH [17.58], $\text{Co}(\text{OH})_2$ [17.59], Cu [17.60], and Cu_2O [17.38, 48]. However, complete two-beam analysis of the dislocation and invisibility criterion has only been carried out for a smaller set of materials including PbS, CdSe, and Cu. The stability of the nanomaterials under high-vacuum and high-energy electron beam conditions inside the TEM, and the tilting angle range of the TEM goniometer are two main limiting factors to achieve a complete two-beam analysis.

17.3.2 Determination of Eshelby Twist

Various techniques based on TEM and electron diffraction have been established to identify and quantify the Eshelby twist. The most intuitive method relies on the

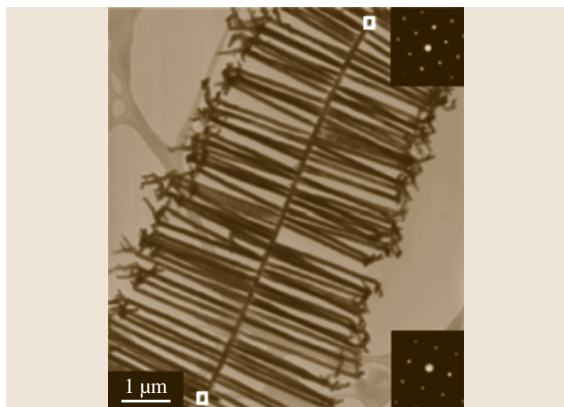


Fig. 17.8 TEM image of a single chiral branched NW. White boxes indicate the positions at which the CBED patterns were acquired. Upper inset: CBED pattern obtained at the top box showing [110] zone axis. Lower inset: CBED pattern obtained at the bottom box showing [100] zone axis (after [17.40])

variation of the electron diffraction on different regions of a NW caused by the rotation in the crystal lattice. Convergent-beam electron diffraction (CBED) is often chosen to acquire diffraction patterns due to its small probe area, which can minimize the interference caused by lattice rotation. In brief, the electron probe is moved along the NW's axial direction to find two distinct zone axes. The twist angle can be calculated by dividing the angular separation between the two identified zone axes by the spatial separation between the two probed areas; For example, starting with the end of the PbSe NW on the [100] zone axis (bottom of Fig. 17.8), the diffraction pattern continuously rotates about the (001) reflection as the probe moves along the wire, reaching the [110] zone axis (top of Fig. 17.8) [17.40]. These two spots are separated by $9.1 \mu\text{m}$ along the NW axis, while the [100] and [110] directions are 45° apart in the cubic structure, which gives approximately $5^\circ/\mu\text{m}$ twist of the lattice. The NW has a diameter of 96 nm , which leads to a calculated value of $b = 0.624 \text{ nm}$. This method, however, requires the NW to have a relatively large twist angle and/or length so that both zone axes are observable. In addition, this measurement is inaccurate in the presence of other geometrical distortion of the lattice, e.g., bending, because this also affects the orientation of the lattice planes and the consequent electron diffraction.

The twist contour analysis reported by Drum in 1965 provides an alternative and more accurate method to determine the sense and magnitude of the twist in crystals [17.37]. Unlike the previously discussed

method based on CBED, twist contour analysis is essentially a diffraction-contrast TEM technique. First, twist contours must be differentiated from the bend contours commonly observed in TEM of nanomaterials. Bend contours, as the name suggests, occur when a NW is bent about its axis. This distorts many atomic planes locally at the bend, causing the diffraction of electrons from this region of the crystal to be different from everywhere else. Therefore, when a zero-beam bright-field TEM image is taken of a bent object, because electrons are diffracted in such a way that virtually none of them remain in the zero beam, the bend contour appears very dark compared with everywhere else. In contrast, when real-space crystal lattice twists along the growth axis cause the reciprocal-space lattice to twist simultaneously, the various reciprocal \mathbf{g} vectors that are orthogonal to the NW growth axis come on and off the Laue condition at different angles, creating several twist contour bands. If we generically choose $-\theta$ for $-\mathbf{g}$ and $+\theta$ for $+\mathbf{g}$, which we will call θ_- , \mathbf{g}_- and θ_+ , \mathbf{g}_+ , respectively, the difference between the two angles $\Delta\theta$ can be calculated geometrically using the relation

$$\Delta\theta = (\theta_+ - \theta_-) = \left(\frac{\lambda}{2}\right) |g_+ - g_-|, \quad (17.11)$$

where λ is the electron wavelength (the inverse of k). Note that the approximation $\theta \approx \lambda g/2$ is made because of the large radius of the Ewald sphere for electron diffraction. For a twisting NW, the upper and lower conditions in Fig. 17.9b can be simultaneously met at different points along the NW, and the resulting twist contours can be imaged using zero-beam bright-field TEM and indexed directly using displaced-aperture dark-field TEM. Unlike bend contours, each of these twist contours is associated with one set of planes and can be easily differentiated. The measured real-space distance L between two indexed twist contours can be used to calculate the real-space twist α , effectively the Eshelby twist, of the NW using the following relation:

$$\alpha = \left(\frac{\Delta\theta}{L}\right) = \left(\frac{\lambda}{2L}\right) |g_+ - g_-|. \quad (17.12)$$

In practice, any \mathbf{g} vectors that are not parallel to the NW growth axis (which contains the orthogonal component) can be selected for the twist contour analysis. An angle correction is needed in this case, and (17.12) needs to be modified to

$$\alpha = \frac{\lambda}{2L} \left| \frac{g_+ - g_-}{\sin \beta} \right|, \quad (17.13)$$

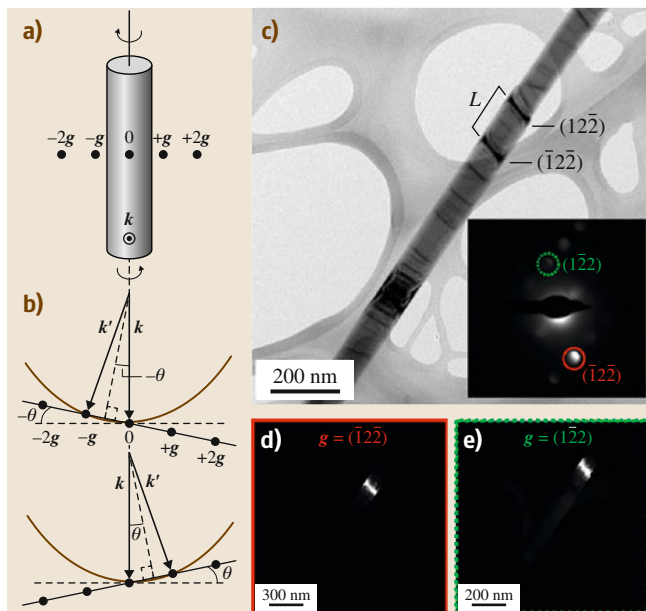


Fig. 17.9a–e Observation and determination of Eshelby twist using twist contours. **(a)** Schematic illustration of a NW showing g vectors orthogonal to the growth axis and the k vector of the electron beam. **(b)** Conditions where $-g$ and $+g$ vectors (top and bottom diagrams, respectively) meet the Laue condition. **(c)** Zero-beam bright-field TEM image of a representative NW showing two indexed twist contours and the physical separation L . Inset convergent-beam electron diffraction pattern. **(d, e)** Displaced-aperture dark-field TEM used to index the two labeled contours as $(\bar{1}\bar{2}\bar{2})$ and $(1\bar{2}\bar{2})$ (after [17.47])

where β is the angle between $\pm g$ and the NW growth direction; For example, the ZnO NW shown in Fig. 17.9 was firstly oriented so that a pair of $\pm g$ vectors [$\pm(1\bar{2}\bar{2})$] were selectively illuminated [17.47]. A zero-beam bright-field image (Fig. 17.9c) was then taken to record the locations of the contour bands so that the separations between them could be measured. Next, each twist contour was uniquely indexed to a specific g vector using displaced-aperture dark-field imaging (Fig. 17.9d,e). A pair of twist contour bands are clearly present in the bright-field image (Fig. 17.9c), and they are indexed to $\pm(1\bar{2}\bar{2})$ g vectors, respectively. The calculated twist for the NW shown in Fig. 17.9c is approximately $9^\circ/\mu\text{m}$ using (17.13), which is in agreement with the Eshelby twist predicted for a NW with radius of 46 nm and Burgers vector's magnitude of approximately 1.0 nm.

In practice, using twist contours to quantify Eshelby twist is much more easily implemented on NW samples than the other techniques discussed above, and

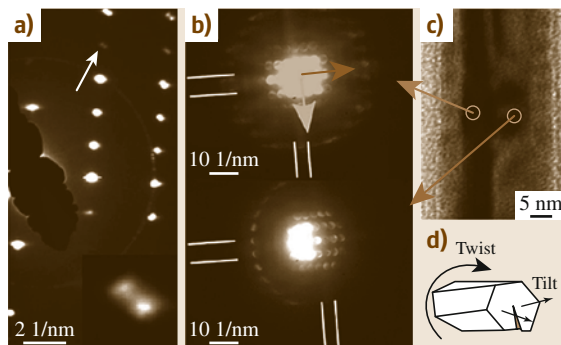


Fig. 17.10a–d Quantification of the lattice tilt using TEM and electron diffraction. **(a)** SAED showing the splitting of the diffraction spots (inset shows the split spot indicated by the arrow, scale 0.21 nm^{-1}). **(b)** CBED patterns showing the tilt of the structure from the left (above) to the right part (below) of the section of the NW. **(c)** Bright-field (BF) image showing the positions of measurement (brown circles) for each CBED pattern. The dark-brown arrow indicates the twist axis, while the light-brown arrow indicates the tilt axis in **(b)**. This is shown schematically in **(d)**. The Kikuchi bands observed have been used to measure the tilt angle (after [17.61])

twist contour analysis can quantify twist of $\approx 1^\circ/\mu\text{m}$ or less, which is a much higher resolution than the other techniques [17.18, 40, 41]. Eshelby twist has been conclusively observed for NWs or NTs of PbS [17.18, 39], PbSe [17.40], CdS, CdSe [17.57], AlN [17.37], ZnO [17.20, 47], Fe: ZnO [17.62], Er: ZnO [17.63], α -FeOOH [17.58], Cu [17.60], and Cu_2O [17.48].

17.3.3 Lattice Tilt

The screw dislocation not only causes the atomic planes to form a helicoid but also splits the crystal lattice at its core. As a consequence, the normal to the basal planes of a dislocated NW is slightly tilted in relation to the growth axis. The degree of tilt ϕ between planes on opposite sides of the screw dislocation is a function of the pitch of the helicoid, which is essentially equal to the magnitude of the Burgers vector b , and the radial position R of the measurement point

$$\cos(\phi) = \frac{1 - (b/(2\pi R))^2}{1 + (b/(2\pi R))^2} \quad (17.14)$$

Therefore, the magnitude of the Burgers vector can be derived from the tilt ϕ and R values [17.61].

Electron diffraction techniques including selected-area electron diffraction (SAED) and convergent-beam

electron diffraction (CBED) are convenient ways to determine the tilt angle ϕ . SAED usually illuminates a large area on the NW sample (hundreds of nanometers) and averages the tilt over all radial positions. The resulting pattern exhibits splitting of diffraction spots because the atomic plane normal is slightly tilted away from the NW axis. The angle of splitting in the diffraction spots is the same as that of the tilt ϕ . The average radial position R can be approximately estimated using one-half of the radius of the NW; For example, the InP NW shown in Fig. 17.10c has a radius of 12.0 nm, and its corresponding diffraction pattern (Fig. 17.10a) shows 2.0° splitting; thus the Burgers vector is calculated to be 0.69 nm, which is approximately one unit cell length of InP [17.61].

CBED, in contrast, measures the local lattice distortion due to its small probe size. The CBED pattern changes abruptly on different sides of the screw dislocation, which is visualized as a shift (Δk , in nm^{-1}) of the Kikuchi bands in reciprocal space (Fig. 17.10b). Therefore, the tilt angle ϕ can be derived from

$$\phi \approx \tan(\phi) = \frac{\Delta k}{k}, \quad (17.15)$$

where k is the wavevector of the incident electron beam. The radial position R is determined from the area being analyzed. Because NWs are thin objects, lower practical electron beam energy is preferred to make the Kikuchi bands visible. Using this CBED technique to determine the Burgers vector of the same NW shown in Fig. 17.10 returns a similar value (0.7 nm) to that obtained by the SAED technique. This measurement of lattice tilt is a newly developed technique, and has only been implemented for InP NWs [17.61].

17.3.4 Observation of Nanotubes or Voided NWs

As discussed earlier, the template-free, spontaneous formation of single-crystal inorganic NTs is a consequence of growth driven by screw dislocations with large Burgers

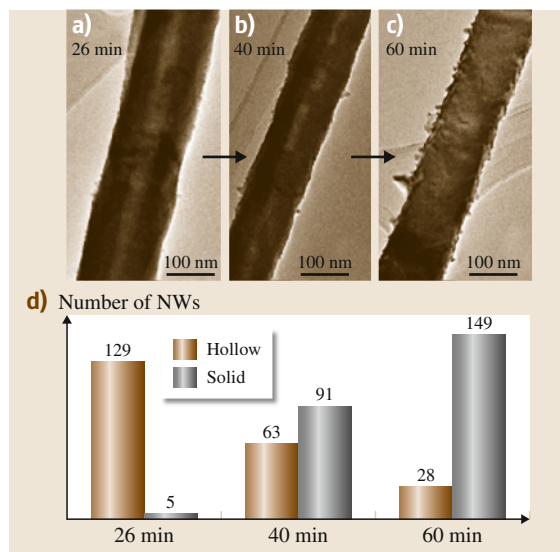


Fig. 17.11a–d Growth history of Cu_2O NTs and NWs revealed by TEM examination of the products with different growth times. (a) The completely hollow NT product from a 26 min reaction, (b) the partially hollow product from a 40 min reaction, and (c) the solid NW product from a 60 min reaction; (d) statistics of the observed Cu_2O NTs and NWs at different reaction times (after [17.48])

ers vectors. The NT can be conveniently visualized under TEM, as the core of the NT appears brighter than the wall due to the greater electron transmission.

In addition to NT structures whose interior is completely hollow, partially filled tubes and NWs with voids also imply the operation of the dislocation-driven mechanism; For example, investigating the growth time effect on Cu_2O NW growth revealed that the 1-D structures are almost exclusively hollow NTs at the beginning, and then were gradually filled up to become voided NWs and eventually solid NWs (Fig. 17.11) [17.48]. Hollow or voided structures have been observed in NWs/NTs of GaN [17.64], ZnO [17.20], $\alpha\text{-FeOOH}$ [17.58], Cu [17.60], Cu_2O [17.48], AlN [17.65], and In_2O_3 (doped or undoped) [17.66–68].

17.4 Generality of Dislocation-Driven Nanomaterial Growth

In this section we review a variety of different anisotropic nanomaterials whose growth has been proven to be driven by screw dislocations in contemporary nanomaterial literature and thus demonstrate

the generality of the dislocation-driven mechanism. The material classes of the nanomaterials known to form via the dislocation-driven mechanism vary from metal, metal oxide/hydroxide, metal chalcogenide, to

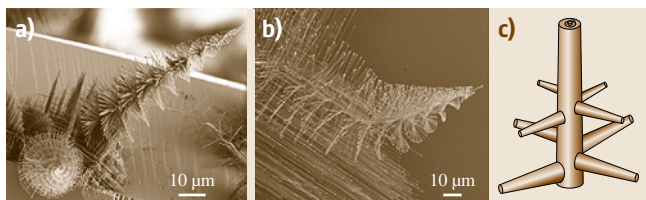


Fig. 17.12a–c Screw-dislocation-driven growth of PbS tree-like NWs. (a,b) SEM images of pinetree-like PbS NWs. (a) Schematic illustration to explain the growth of the pinetree structure: the trunk's growth is driven by axial screw dislocation and that of the branches by VLS (after [17.19])

metal nitride; the chemistry involved in forming the dislocation-driven nanomaterials can be distinctly different, ranging from simple hydrolysis reaction to reduction–oxidation (redox) reaction, and dislocation-driven growth can be accomplished in both vapor phase and solution phase. Despite the diversity in the physical and chemical properties of these nanomaterials, the rule of thumb in pursuit of rational synthesis of anisotropic nanomaterials is to maintain low supersaturation of the precursor to favor the dislocation-driven mechanism. We also present evidence of the dislocation-driven mechanism for each material using methods reviewed in the previous section.

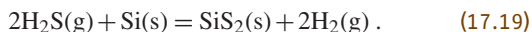
17.4.1 Vapor-Phase Synthesis

The growth of NWs in vapor phase has been almost exclusively explained by the VLS and other analogous catalyst-driven mechanisms. The dislocation-driven crystal growth mechanism has long been underappreciated because of the easy visualization of a catalyst particle decorating the tip of the NW, whereas the TEM techniques to detect dislocations are not straightforward. Even in cases where catalyst particles were absent yet NW growth still occurred, researchers used to claim that the 1-D anisotropic growth was driven by self-catalyzed VLS. It should be cautioned that the role of dislocation-driven growth needs to be reexamined in these cases. Even in the presence of catalyst particles, there is still the possibility of the cooperation of both mechanisms. It is likely that, without the presence of catalyst nanoparticles, there is a higher energy barrier to nucleation of NW growth, therefore causing the low yield and slow growth rate of NWs that are commonly observed. Addition of catalyst nanoparticles promotes nanostructure growth with high yield by creating numerous nucleation sites, and thus facile and fast 1-D crystal growth is initiated. Furthermore, addition of

catalyst impurities and the fast and disordered crystal growth could potentially lead to the generation of dislocation sites that further facilitate the crystal growth process, which might become more responsible for the subsequent NW growth under the low supersaturation level.

PbS

PbS pinetree-like NWs were the first reported case of dislocation-driven growth among the modern NWs (Fig. 17.12a,b). Nanostructures of PbS are synthesized via chemical vapor deposition using PbCl₂ and elemental sulfur as precursors under argon flow with a co-flow of H₂ at atmospheric pressure and with temperatures of 600–650 °C [17.18, 39]. A piece of freshly exposed Si substrate is used to collect the NW product. The formation of the tree structure is indeed a combined effect of the operation of both the dislocation-driven NW growth mechanism and the VLS mechanism: the growth of the trunks is driven by axial dislocations, whereas the branches are formed via in situ VLS growth, as illustrated in Fig. 17.12c. The hydrogen flow plays an important role in triggering the dislocation-driven growth of the tree trunks. The chemical reactions involved are



The onset of hydrogen flow likely creates a spike in H₂S supersaturation and initiates dislocations with screw components that then propagate anisotropically to form the NW trunks. Maintaining an optimum hydrogen flow can provide a favorable supersaturation that promotes dislocation-driven trunk NW growth and enable the simultaneous growth of the VLS-driven NW branches.

PbSe

PbSe tree-like NWs (Fig. 17.8) have also been reported [17.40]. The synthesis of PbSe NWs was analogous to that of PbS due to their structural similarity, though some minor details of the chemical vapor deposition (CVD) precursors vary. Again, screw dislocation is responsible for the trunk growth, and VLS for the branch growth. One different aspect in the PbSe synthesis is that an intentional metal catalyst, bismuth in this case, was used, yet no obvious catalyst cap on the NW trunk was observed. This agrees with the hy-

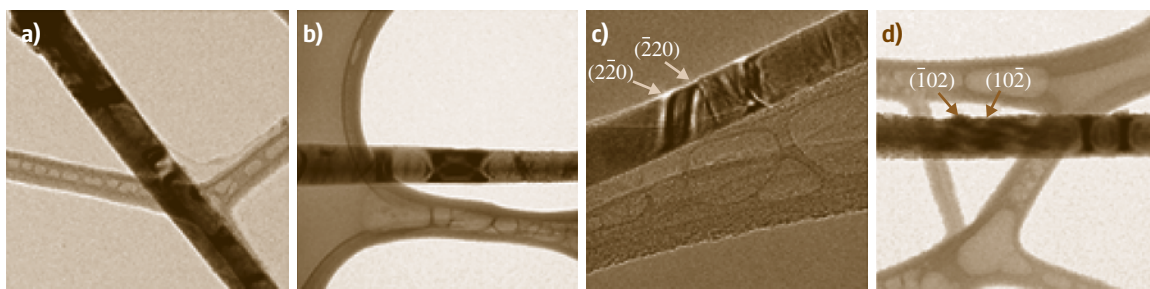


Fig. 17.13a–d Evidence of dislocation-driven growth of CdS and CdSe NWs. Dislocation contrast of a CdS NW (a) and a CdSe NW (b), and twist contours on a CdS NW (c) and a CdSe NW (d) (after [17.57])

pothesis that metal particles might serve to facilitate dislocation-driven growth rather than acting as a VLS catalyst.

CdS/CdSe

CdS and CdSe share the wurtzite crystal structure, which is considered to be dislocation prone. There have been early reports on the dislocation structures in CdS/CdSe whiskers and ribbons [17.69–71]. Recently, CdS or CdSe NWs were grown via the chemical vapor deposition (CVD) process using CdCl₂ and elemental sulfur/selenium as precursors under argon flow with a co-flow of H₂ at relatively low system pressure of 40 Torr at temperatures of 600–650 °C [17.57]. Si substrates, either covered with gold nanoparticles or not, were used to collect the products. With the presence of gold nanoparticles, NWs with high yield and uniformity were obtained. Interestingly, even when the gold nanoparticle catalyst was absent, short NWs could still be grown. The vapor pressure was low in this reaction compared with most of the other reported CVD synthesis conditions [17.72–74], thus favoring dislocation-driven crystal growth.

Evidence for dislocation-driven growth was indeed detected in the NWs synthesized with the presence of gold nanoparticles. Dislocation contrast was observed in both as-synthesized CdS (Fig. 17.13a) and CdSe (Fig. 17.13b) NWs, and the Burgers vectors of the dislocation were determined to be [120] for CdSe under strong two-beam conditions. Moreover, twist contour analysis revealed the presence of Eshelby twist associated with the dislocation in both CdS (Fig. 17.13c) and CdSe (Fig. 17.13d) NWs.

These results clearly showed that dislocation-driven NW growth had occurred during the CVD growth of CdS and CdSe NWs, even when gold nanoparticle catalysts were employed for the synthesis, suggesting that both VLS growth and the dislocation-driven growth

mechanism can coexist in the growth of 1-D CdS and CdSe NWs.

AlN

AlN whiskers were one of the earliest examples whose growth was demonstrated to be driven by screw dislocation. Back in 1965, Drum et al. observed the dislocation contrast running through AlN whiskers and developed the twist contour analysis to verify the presence of Eshelby twist in these whiskers (Fig. 17.14a) [17.37]. More recently, hollow AlN NTs (Fig. 17.14b) were synthesized by nitridization of Al metal powder in the presence of Co(III) salts [17.65]. The spontaneous formation of the NT structure is highly suggestive of screw-dislocation-driven growth.

GaN

GaN NWs were synthesized by catalyst-free direct reaction of gallium vapor and ammonia at 1000 °C [17.64]. Cross-sectional investigation (Fig. 17.15) of these NWs revealed the presence of nanopipes. Particularly cross-

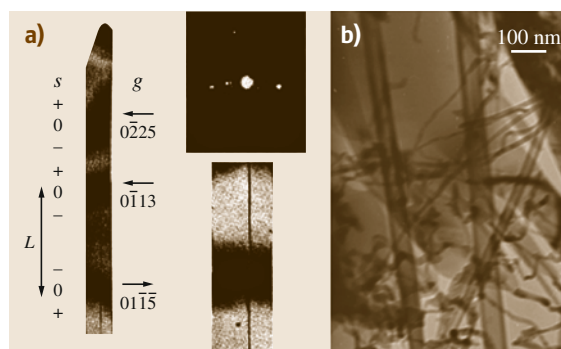


Fig. 17.14a,b Screw-dislocation-driven growth of AlN NWs. (a) Twist contour analysis of AlN whiskers; the dislocation contrast was also clearly observed (after [17.37]); (b) TEM image of AlN NTs (after [17.65])

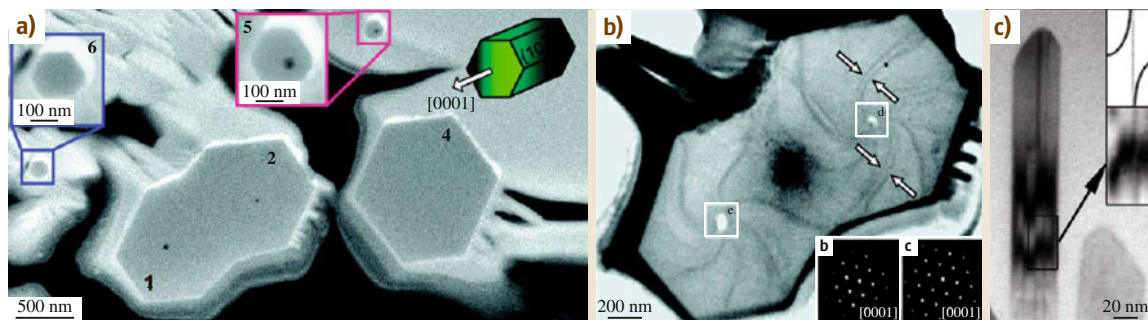


Fig. 17.15a–c Screw-dislocation-driven growth of GaN NWs and NRs. (a,b) Cross-sectional SEM (a) and TEM (b) images of GaN NWs with nanopipes in the middle (after [17.64]). (c) TEM image of a GaN NR displaying dislocation contrast (after [17.75])

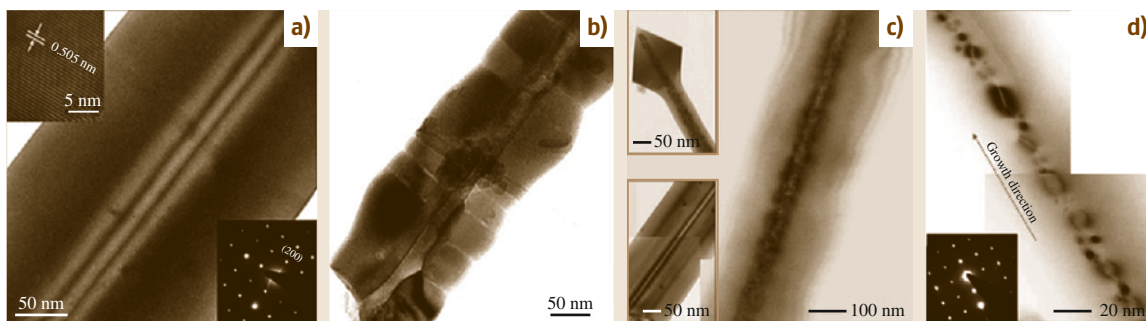


Fig. 17.16a–d Screw-dislocation-driven growth of undoped and doped In_2O_3 NTs. (a,b) TEM images of undoped In_2O_3 NTs; (c,d) TEM images of Sn-doped In_2O_3 NWs that display voids and dislocation loops (after [17.68, 68])

sectional TEM imaging (Fig. 17.15b) shows interesting spiral bend contours, which were believed to be associated with screw dislocations with large Burgers vectors. This is consistent with the mechanism of NT formation that was discussed previously.

GaN NRs grown by molecular-beam epitaxy were also reported to display dislocation contrast (Fig. 17.15c) [17.75].

$\text{In}_2\text{O}_3/\text{Sn}:\text{In}_2\text{O}_3/\text{Zn}:\text{In}_2\text{O}_3$

In_2O_3 NWs were synthesized using simple thermal evaporation of InN powder at ambient condition [17.66]. Sn/Zn doping was introduced by mixing InN and SnO_2/ZnO powder followed by a similar evaporation process [17.67, 68]. The resulting undoped 1-D In_2O_3 nanostructures were indeed hollow nanopipes (Fig. 17.16a,b), which is one of the characteristics of dislocation-driven growth. More intriguingly, the doped NWs exhibited curious features such as nanoprecipitates, voids, and dislocation loops (Fig. 17.16c,d). It is likely that the formation of the nanopipe to relieve the dislocation strain energy can be locally affected by the

presence of dopants around the dislocation and the formation of nanoprecipitates and loops, leading to the observed discontinuous nanopipe.

Fe:ZnO/Er:ZnO

Fe-doped ZnO NWs were synthesized by thermal evaporation of a mixture of ZnS and Fe_2O_3 powder [17.62]. Eshelby twist was detected using twist contour analysis (Fig. 17.17a), which supports the dislocation-driven growth of these NWs.

Er-doped ZnO tree-like NWs were synthesized using a similar thermal evaporation method except that the precursors were ZnO and Er_2O_3 [17.63]. The twist of the NW trunk was evidenced by the rotation of the branches, which is indicative of the dislocation-driven growth of the trunk (Fig. 17.17b,c).

17.4.2 Solution-Phase Synthesis

Direct Hydrolysis

The hydrolysis reaction is probably one of the simplest types of chemical reactions, yet it is a versatile

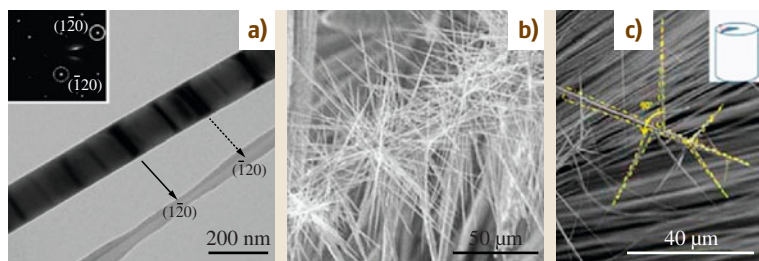


Fig. 17.17a–c Screw-dislocation-driven growth of undoped and doped ZnO NWs. **(a)** Twist contour analysis of an Fe : ZnO NW (after [17.62]) and **(b,c)** SEM images of tree-like Er : ZnO NWs (after [17.63])

route to produce many important metal oxides at large scale in low-temperature aqueous solutions. ZnO, the first solution-grown dislocation-driven nanomaterial to be demonstrated, was synthesized via direct hydrolysis of Zn^{2+} in the presence of hexamethylenetetramine (HMT) as the precipitation reagent and pH buffer [17.20]. The details of the synthesis and characterization of ZnO have been discussed in previous sections. This example provides the general framework for designing the rational synthesis of anisotropic nanomaterials driven by screw dislocations. The understanding on how to control the concentration of the precursor metal ions and therefore the supersaturation level for hydrolysis in order to favor dislocation-driven crystal growth kinetics may enable rationally designed low-cost NW/NT production for practical applications. In many cases, the direct products of the hydrolysis reactions are metal oxyhydroxides and hydroxides, depending on their surface energetics, size, and environment [17.76], so that a secondary, thermal annealing treatment might be needed to form the desired metal oxides.

Iron Oxyhydroxide. Iron oxyhydroxide (FeOOH) NWs were synthesized using a continuous flow reactor (CFR) with flow of low-concentration FeCl_2 aqueous solution and co-flow of iron microparticles [17.58]. The CFR allows a *constant* low supersaturation level and enables indefinite growth time for the NWs. The contrast between the product morphologies seen for a CFR reaction and a static hydrothermal reaction with comparable conditions is drastic: there are copious amounts of fairly uniform NWs (Fig. 17.18a) for the CFR reactions, while the static hydrothermal reaction yields mainly microparticles with sparse NW growth (Fig. 17.18b). Defective particles were still produced at the initial stage of the growth where a spike of precursor supersaturation occurred, likely providing the source of dislocations, as evidenced by the observation of the seed particles at the end of the NWs (Fig. 17.18b, inset). Dislocation contrast (Fig. 17.18c), Eshelby twist

(Fig. 17.18d), and hollow structures were readily observed using TEM, confirming the dislocation-driven growth of these NWs.

The hydrolysis reaction to form FeOOH is



Direct hydrolysis of low-concentration Fe^{3+} solution seems to be the most intuitive way to gain good control of the supersaturation. However, the problem is that the hydrolysis of Fe^{3+} is so favorable (K_{sp} for $\text{Fe}(\text{OH})_3 = 4 \times 10^{-38}$) and fast that preventing such favorable hydrolysis (high supersaturation) requires an

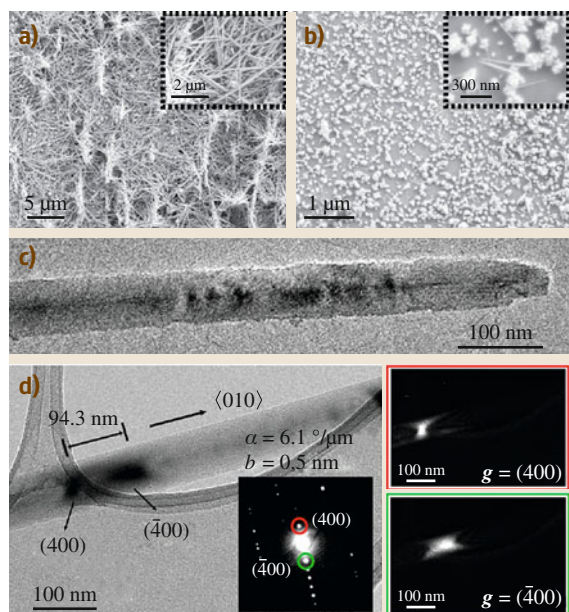
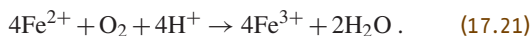


Fig. 17.18a–d Screw-dislocation-driven growth of α - FeOOH NWs. **(a)** SEM images of α - FeOOH NWs yielded from a CFR reaction. **(b)** SEM images of α - FeOOH NWs yielded from a static hydrothermal reaction. **(c,d)** TEM characterization of α - FeOOH NWs. **(a)** Zero-beam bright-field image showing the dislocation contrast. **(d)** Twist contour analysis of an α - FeOOH NW

extreme low pH. In contrast, Fe^{2+} ions do not hydrolyze and precipitate significantly even at near-neutral pH because the K_{sp} for $\text{Fe}(\text{OH})_2$ is 8×10^{-16} , but they can be readily oxidized to Fe^{3+} by dissolved oxygen in the aqueous solution,



Secondly, the presence of Fe metal can reduce Fe^{3+} back to Fe^{2+} ions and therefore guarantee a low concentration (supersaturation) of Fe^{3+} as dictated by the $\text{Fe}^{3+}/\text{Fe}^{2+}$ redox equilibrium,



By coupling these two *protection* schemes (low-concentration flow and redox equilibrium) to the original hydrolysis reaction, a low supersaturation of Fe^{3+} ions can be maintained to guarantee slow and controlled hydrolysis, which favors dislocation-driven 1-D crystal growth. Unlike other reports of iron oxide/oxyhydroxide nanomaterial syntheses where either surfactants or organic ligands were used and argued to be important in the NW synthesis [17.77–80], this method merely requires the simple inorganic precursors Fe^{2+} and Fe.

Co(OH)₂. Co(OH)₂ NWs are an intermediate product during the synthesis of Co₃O₄ NWs, where cobalt nitrate is hydrolyzed in the presence of concentrated ammonia ($\text{NH}_3 \cdot \text{H}_2\text{O}$) [17.59]. The Co(OH)₂ NWs started to grow 2 h after initiation of the reaction. NH_3 can form a series of complex compounds with Co^{2+} ions, and thus a concentrated NH_3 environment effectively reduces the concentration/supersaturation of the free Co^{2+} ions to favor dislocation-driven growth. Dislocation contrast was clearly observed in the as-synthesized Co(OH)₂ NWs under TEM (Fig. 17.19). Unfortunately rigorous two-beam and twist contour analysis were not available, likely due to instability

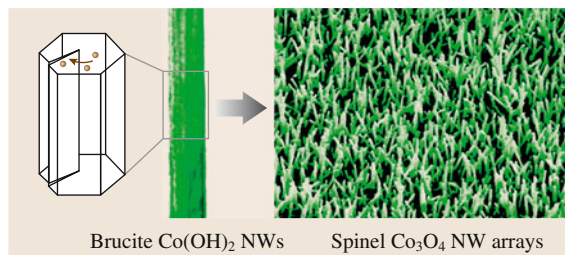


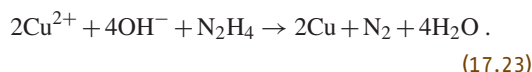
Fig. 17.19 Schematic illustration of dislocation-driven growth of Co(OH)₂ NWs and their conversion into Co₃O₄ NWs (after [17.59])

of the hydroxide species under vacuum and the high-energy electron beam.

Redox Reaction

In contrast to hydrolysis reactions where single precursor ions account for the supersaturation level of the system, in a redox reaction the supersaturation is necessarily determined by both the reducing reagent(s) and the oxidizing reagent(s). Thus, using the concentration of the precursors to describe the supersaturation level in a redox system becomes ambiguous. Indeed, in this case, the best way to represent the equilibrium position of the chemical reaction (and crystal growth) is the electrochemical potential: chemical equilibrium is reached when the electrochemical potential of the reaction is zero. The supersaturation of the redox reaction system is simply the electrochemical overpotential. By tuning the electrochemical potential to be slightly over zero, the low-supersaturation condition is achieved, which favors the dislocation crystal growth regime. The necessity for multiple reactant species increases the complexity of controlling the supersaturation; nevertheless, by understanding this complexity, we can achieve better control of the supersaturation of such redox reactions to promote dislocation-driven NW growth.

Copper (Cu) NWs. Cu represents an entirely different class of materials, metals, which again demonstrates the generality of the dislocation-driven growth mechanism. Cu NWs were initially synthesized by reducing Cu^{2+} ions using hydrazine (N_2H_4) in the presence of ethylenediamine (EDA) and concentrated sodium hydroxide (7 M NaOH) in a closed vial [17.60]. The main reaction taking place to form Cu NWs is



The OH^- ion plays dual roles in the reaction: firstly, it provides a suitable pH condition that allows the redox reaction to occur (the electrochemical potential is dependent on the solution pH); and secondly, it is intrinsically a ligand that can complex with Cu^{2+} to form $\text{Cu}(\text{OH})_4^{2-}$. This complexation lowers the activity (supersaturation) of the Cu^{2+} ions, which promotes the dislocation-driven growth mechanism. Moreover, EDA is a strong complexing ligand (rather than a surfactant) capable of binding with Cu^{2+} , thus further lowering the supersaturation of the system.

Dislocation contrast was observed in many as-synthesized Cu NWs. Rigorous TEM analysis under

strong two-beam conditions characterized the Burgers vector direction of the dislocation to be $[110]$, which is a pure screw dislocation (Fig. 17.20). Twist contour analysis confirmed the presence of an Eshelby twist structure and quantified the magnitude of the Burgers vector to be $1/2 [110]$, which is the most common Burgers vector in the face-centered cubic (fcc) structure [17.27]. Furthermore, hollow NTs of Cu were present occasionally.

Understanding of the dislocation-driven growth of Cu NWs allows improved synthesis under a much milder chemical environment. The static reaction (17.23) has two drawbacks: firstly, an extremely high concentration of NaOH (7 M) is required; and secondly, NW lengths are limited due to precursor depletion. Understanding and controlling the supersaturation of the crystal growth is the key to promote dislocation-driven growth. For the redox reaction between Cu^{2+} and N_2H_4 , the change in the free Cu^{2+} ion concentration only affects one half-cell reaction for supersaturation control. Tuning the concentration of N_2H_4 also influences the supersaturation of the reaction system. One of the roles of NaOH is complexing Cu^{2+} and reducing the concentration of free Cu^{2+} ions; thus, by compensating the reduction in NaOH concentration with an increase in the other complexing ligand, EDA, low supersaturation can be maintained and successful dislocation-driven NW growth can still be achieved. Indeed, a modified static reaction with a much lower concentration of NaOH ($\text{pH} \approx 12$) still led to the formation of Cu NWs. Since EDA is a much stronger ligand ($\beta[\text{Cu}(\text{EDA})_2] = 10^{20}$) than OH^- ($\beta[\text{Cu}(\text{OH})_4^{2-}] = 10^{16}$), a modest increase in EDA concentration can sufficiently compensate for a two order of magnitude drop in NaOH concentration. Furthermore, according to reaction (17.23), OH^- ions participate in the redox reaction that forms Cu, thus reducing the NaOH concentration also lowers the redox overpotential and crystal growth supersaturation, thus favoring dislocation-driven growth. NWs yielded from this protocol are typically $\approx 5 \mu\text{m}$ in length and 200–300 nm in diameter with slight tapering (Fig. 17.21a,b), indicating that precursor depletion occurs as the reaction proceeds. The precursor depletion problem could be solved using a CFR, which yielded much longer Cu NWs (about $30 \mu\text{m}$ on average, up to $50 \mu\text{m}$, Fig. 17.21c,d) with uniform diameter distribution.

Cuprous Oxide (Cu_2O) NWs. Natural Cu_2O (cuprite) mineral whiskers were among the earlier examples where axial screw-dislocation contrast was clearly observed in

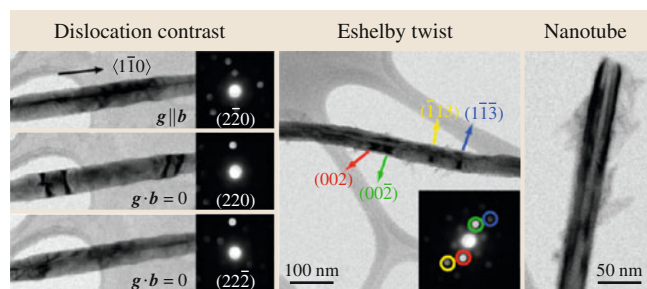


Fig. 17.20 TEM evidence proving the dislocation-driven growth of Cu NWs/NTs (after [17.60])

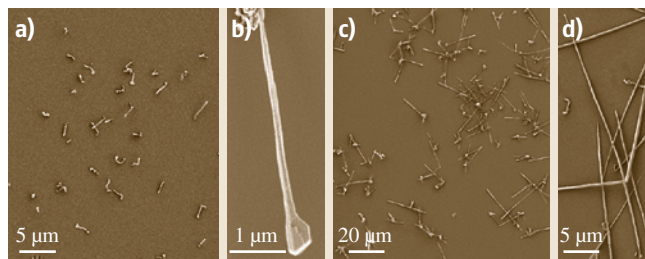


Fig. 17.21a–d Improved synthesis of Cu NWs. SEM images of Cu NWs synthesized under modified conditions via static reaction (a,b) or CFR reaction (c,d) (after [17.60])

TEM [17.38]. Recently, Cu_2O NWs were synthesized using a low-concentration Fehling's reaction where Cu^{2+} ions were reduced by glucose in the presence of sodium hydroxide and sodium tartrate [17.48]. The formation of the Cu_2O in solution is similar to that of Cu in terms of the redox chemistry. However, glucose is a much weaker reducing reagent, so Cu(II) can only be reduced to Cu(I) species. Tartrate forms a Cu^{2+} -tartrate coordination complex ($K_f \approx 10^7$) that both prevents $\text{Cu}(\text{OH})_2$ precipitation and serves to reduce the concentration of free Cu^{2+} ions, lowering the supersaturation to promote dislocation-driven NW growth.

TEM characterization of these NWs only detected a few of them with dislocation contrast, since most of the NWs were actually formed by filling up the initially formed Cu_2O NTs (Fig. 17.22). Besides the dislocation contrast and spontaneous formation of NTs, the observation of the Eshelby twist in these NTs/NWs also confirms that their growth is driven by screw dislocations.

17.4.3 Solution Growth of 2-D Nanoplates

As discussed earlier, the spiral step edges generated by screw dislocations can be chemically modified, re-

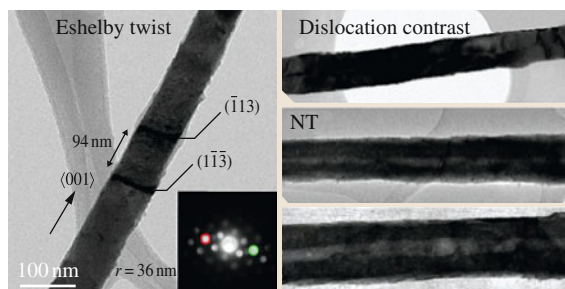


Fig. 17.22 TEM evidence proving the dislocation-driven growth of Cu_2O NWs/NTs (after [17.48])

sulting in disparate step velocities. This is the key to achieve desirable anisotropic growth driven by screw dislocations. Despite the drastic differences in morphologies between 1-D NWs/NTs and 2-D nanoplates, dislocation-driven crystal growth is common to both

and the subtle kinetics of spiral step propagation associated with dislocation growth can be used to explain each. The characterization of dislocation-driven 2-D nanomaterial is more straightforward as the spiral step edges lying on the basal plane of the nanoplates can be directly observed using both scanning electron microscopy (SEM) and atomic force microscopy (AFM). Dislocation-driven 2-D growth has already been proven to be responsible for the growth of a variety of materials including zinc hydroxysulfate (ZHS), $\text{Co}(\text{OH})_2$, $\text{Ni}(\text{OH})_2$, and gold nanoplates. Here, their synthesis and characterization are discussed.

Zinc Hydroxysulfate (ZHS)

In a typical synthesis of ZHS nanoplates, aqueous solutions containing ZnSO_4 , $\text{Zn}(\text{NO}_3)_2$, and hexamethylenetetramine (HMT) are heated in sealed glass vials [17.50]. A piece of Si substrate is placed in the solution to collect the nanoplate products. SEM re-

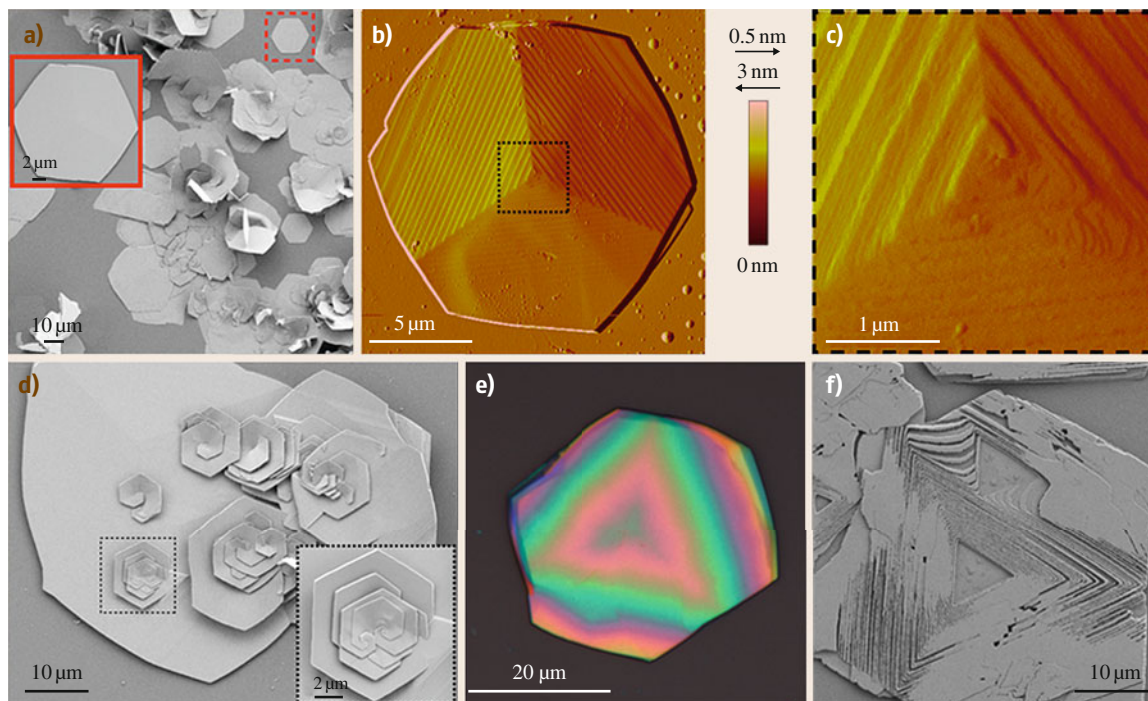


Fig. 17.23a–f Overview of nanoplate morphology and screw dislocation step edges of ZHS. (a) Low-magnification scanning electron microscopy (SEM) image of as-synthesized ZHS nanoplates; *inset* is a representative hexagonal nanoplate. (b) Low-magnification contact-mode AFM image of a representative nanoplate (deflection signal shown). (c) Higher-magnification image of the dislocation core. (d) Large nanoplate containing several screw dislocations of different handedness. (e) Bright-field optical image showing the thin-film interference pattern generated between the nanoplate and the reflective silicon substrate, revealing the radial thickness variations within the nanoplate. (f) SEM image of a nanoplate grown on a silicon substrate with native oxide (after [17.50])

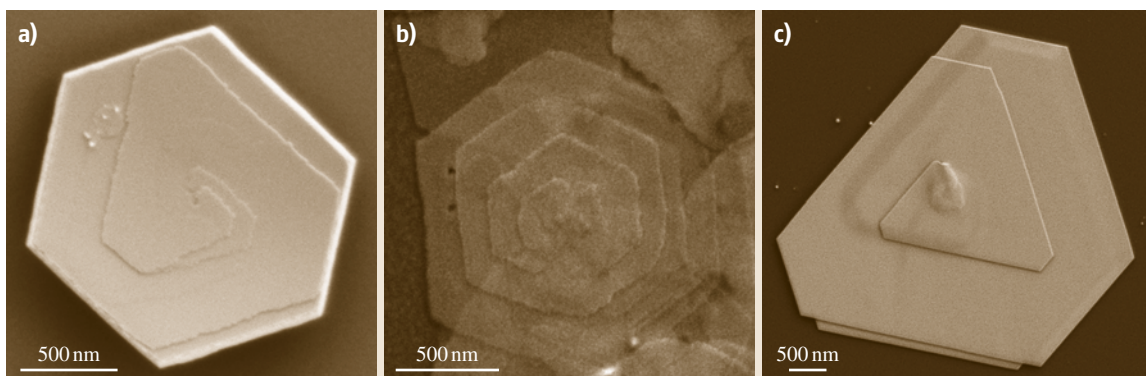


Fig. 17.24a–c Other examples of dislocation-driven nano-plates. SEM images of representative nanoplates of (a) α -Co(OH)₂, (b) Ni(OH)₂, and (c) gold, highlighting the screw dislocation spirals (after [17.50])

vealed that the substrates are densely coated with many nanoplates (Fig. 17.23a) after this reaction procedure. In contrast, in the absence of ZnSO₄, ZnO nanorods are the exclusive reaction product [17.81, 82]. All of these nanoplates were found to contain screw dislocations using contact-mode AFM. For the representative hexagonal morphology, these dislocations were single-source dislocations and the core was located at the very center of the nanoplate (Fig. 17.23b,c). Interestingly, simple bright-field optical microscopy revealed the thin-film interference pattern generated between the surface of a nanoplate and the reflective silicon substrate surface, which demonstrated the geometry and thickness variation of the nanoplate and the location of the dislocation cores (Fig. 17.23e). Due to the dislocation hillocks, these nanoplates are in fact *pyramids* with extremely high width-to-thickness ratios. Multiple dislocation centers with different chirality were observed in larger and more complex nanoplate morphologies (Fig. 17.23d). Moreover, when nanoplates are grown on silicon surfaces with native oxides, the dislocation spirals are heavily etched, clearly revealing their morphology under standard SEM (Fig. 17.23f). Similar zinc hydroxydodecylsulfate (ZHDS) nanoplates were also reported to grow via the dislocation-driven mechanism [17.83].

Co(OH)₂

Co(OH)₂ nanoplates (Fig. 17.24a) were synthesized via direct hydrolysis of cobalt(II) chloride in the presence

of HMT as the pH buffer [17.50]. The α -Co(OH)₂ samples had high densities of nanoplates that all showed dislocations. However, due to their smaller diameter and wider terrace widths, they did not display the same dramatic thin-film interference under optical microscopy.

Ni(OH)₂

Ni(OH)₂ nanoplates (Fig. 17.24b) were synthesized similarly via direct hydrolysis of nickel(II) acetate in the presence of HMT [17.50]. The Ni(OH)₂ nanoplates were equally dense but thinner than ZHS and exhibited a propensity to form flower-like structures [17.84] similar to the off-shooting nanoplates seen in ZHS (Fig. 17.23a).

Gold

Gold nanoplates (Fig. 17.24c) were synthesized by reducing chloroauric acid (HAuCl₄) in aqueous solution using salicylic acid [17.50]. Consistent with literature [17.85], gold nanoplates form as triangles and hexagons as well as truncated triangles; however, only a small percentage of these plates clearly show dislocation spirals. Moreover, the step heights, previously estimated to be ≈ 100 Å [17.85], and thus the Burgers vectors of the dislocations observed in gold plates, are very large in comparison with the (111) spacing of 2.35 Å for gold. The surface of gold nanoplates is the (111) plane, and this should be the elementary Burgers vector.

17.5 Rational Growth of Dislocation-Driven Nanomaterials – General Strategies

The empirical understanding gained from the examples discussed above provides general guidelines for dislocation-driven nanomaterial growth, which requires two basic ingredients:

1. The presence of dislocation sources (*seeds*) to propagate the growth
2. A suitable low supersaturation condition for promoting dislocation-driven growth over LBL and other crystal growth modes [17.19].

We discuss these two aspects separately.

Manipulation of the supersaturation level to favor dislocation-driven growth of nanomaterials needs

to be specific depending on the chemistry of the materials. In general, an overall low concentration (in solution) or vapor pressure of reactants is preferred. Particularly in solution growth, introduced ligand compounds can complex with free ions of the precursor and thereby effectively reduce the activity (supersaturation) of the reactants. The versatile nature of coordination chemistry can be exploited to rationally tune the supersaturation level to promote dislocation-driven growth. The role of the *surfactants* commonly employed in many solution syntheses might need to be reexamined from the perspective of controlling the supersaturation in the solution system, since many of them are multidentate ligands. Redox chemical equilibrium or other chemical equilibrium systems can also result in a buffering effect and allow the supersaturation level to be effectively controlled. Furthermore, the employment of a continuous flow reactor (CFR) (Fig. 17.25a) can allow better control over the supersaturation than the commonly practiced closed-system growth (referred to as *static growth* later) does. Static growth, where precursors are introduced at the beginning and allowed to react to completion, suffers from a significant decline in precursor concentration (supersaturation) during the course of the reaction (Fig. 17.25b), which leads to irregular growth kinetics that are difficult to deconvolute and control. CFR can maintain a constant low supersaturation targeting the dislocation-driven regime and enable indefinite growth times.

On the other hand, to date, there are few rational routes to engineer the dislocation source. To create dislocation sources, the most common and straightforward approach is to generate defective seed crystals [17.86] under high-supersaturation reaction conditions. Ideally, the seeds are prepared separately from the growth system [17.20]; nevertheless, oftentimes an initial spike of high supersaturation of precursors in the growth system can achieve a similar objective [17.18, 39, 48, 58, 60]. Screw dislocations can also come from other crystalline substrate surfaces, since they are always present in crystals. Screw dislocations in defect-rich substrates, such as GaN thin film grown on sapphire, have been utilized to *seed* dislocation-driven growth of vertically epitaxial ZnO NWs (Fig. 17.26) from solution [17.47]. The density of the ZnO NWs is comparable to the densities of screw dislocations found in such GaN thin films, and NWs are found to grow only from the disloca-

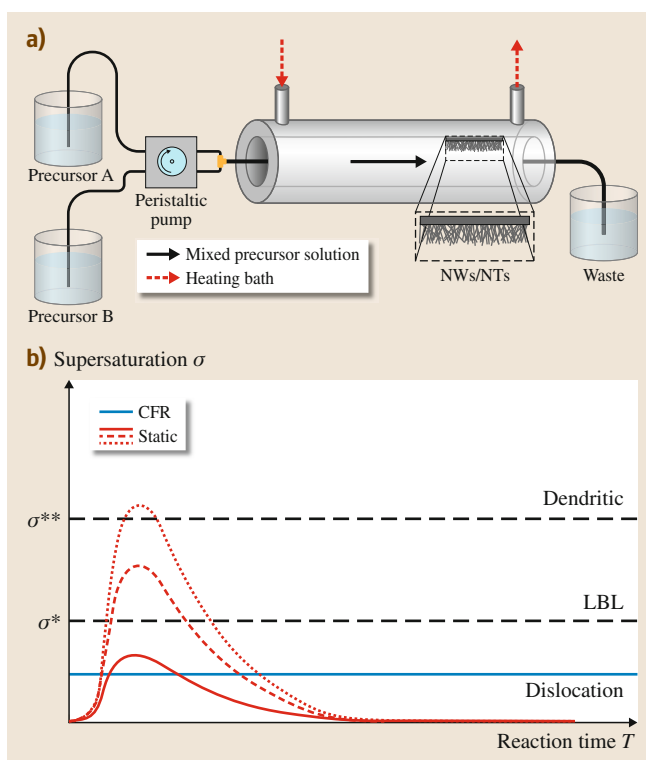


Fig. 17.25a,b Schematic of continuous flow reactor (CFR) and supersaturation profiles. **(a)** Consisting of a jacketed chromatographic column, a heated circulating water bath, and a dual-head peristaltic pump, the CFR enables precise control over reaction temperature, precursor solution composition/flow rate, substrate location, and reaction time (heated circulating water bath not shown). **(b)** Comparison of schematic supersaturation profiles for closed-system reactions and the CFR reaction (after [17.20])

tion etch pits formed on the surface of GaN substrates that have been cleaned aggressively. It is possible that the *seeding layers* of ZnO film or other materials initially formed on various substrates that are crucial for successful growth of NWs of ZnO or other materials could play similar roles; i. e., such *seeding layers* could in fact be the highly defective substrates that contain numerous screw dislocations that then initiate dislocation-driven growth of NWs. Furthermore, this *threading* dislocation growth that propagates from substrate to NW of another material lays the foundation for the creation of NW heterostructures driven by dislocations.

17.6 Applications

The dislocation-driven nanomaterial growth mechanism is a general mechanism that can apply to any material. It does not require catalysts that form eutectics with the targeted nanomaterials and does not depend on the same material compatibility; therefore, more materials can be grown in the anisotropic fashion dictated by the dislocation. Another significant advantage of dislocation-driven growth is that it can be conveniently implemented in low-temperature aqueous solutions, which can lead to less expensive and energy-intensive production of anisotropic nanostructures of many useful materials. Furthermore, dislocation-driven growth operates at low supersaturation, which is essentially the near-equilibrium state. In this sense, the consumption of the precursors is low, so that the synthesis can be more cost-efficient.

Particularly for the significant applications of NWs and NTs in renewable energy, such as solar energy conversion, battery electrodes, and thermoelectrics, large amounts of ecologically sustainable nanomaterials made at low cost are demanded to address the large-scale energy challenges. Some Earth-abundant semiconductor materials that are promising for solar energy and other renewable energy applications suffer from poor mobility, carrier density, or minority carrier diffusion length. For many of these unconventional abundant materials, new design concepts based on nanoscale materials such as NWs may enhance their utility, because the nanoscale dimensions may circumvent their shortcomings or make them much more tolerable for applications [17.6, 87–90].

A good example are the nanomaterials of various iron-based compounds such as α -Fe₂O₃ (hematite,

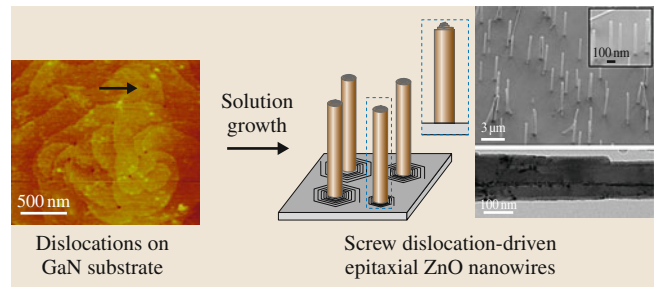


Fig. 17.26 Schematic illustration of dislocation-driven growth of ZnO NWs seeded by screw dislocations in GaN substrates (after [17.47])

bandgap 2.1 eV) [17.89, 91], β -FeS₂ (pyrite, bandgap 0.95 eV) [17.92, 93], and FeF₃ [17.94, 95]. Because iron (Fe) is the fourth most abundant element in the Earth's crust, these compounds have the potential to meet or exceed the annual worldwide energy demand at a significantly lower material production cost over traditional or leading solar materials that are based on rare elements such as indium, gallium, and selenium [17.96]; For example, hematite has been intensively studied because it is a promising photoanode material for catalyzing photoelectrochemical (PEC) water splitting, yet the performance of hematite electrodes still suffers from its poor semiconducting properties [17.89, 91]. NWs of hematite could circumvent its shortcomings, and they can be conveniently converted from screw-dislocation-driven α -FeOOH NWs via thermal annealing [17.58].

Iron fluoride (FeF₃), on the other hand, is a promising high-capacity Li-ion battery cathode material that is much cheaper than the current lithium cobalt oxide (LiCoO₂) cathode material [17.94]. However, such promise has been held back by the slow ionic diffusion and low conductivity of FeF₃. FeF₃·3H₂O NWs have been synthesized following the guideline of dislocation-driven NW growth at gram scale in solution using low-concentration iron(III) nitrate and hydrofluoric acid as precursors (Fig. 17.27a) [17.95]. Due to the high solubility of FeF₃·3H₂O in water (5.92 g/100 g H₂O at 25 °C), ethanol was chosen as the solvent, in which FeF₃·3H₂O dissolves very little [17.97]. F⁻ is a good complexing ligand for Fe³⁺ to make the stable FeF₆³⁻ complex ($K_f = 10^{15.04}$) [17.98], which effectively maintains the low supersaturation environment

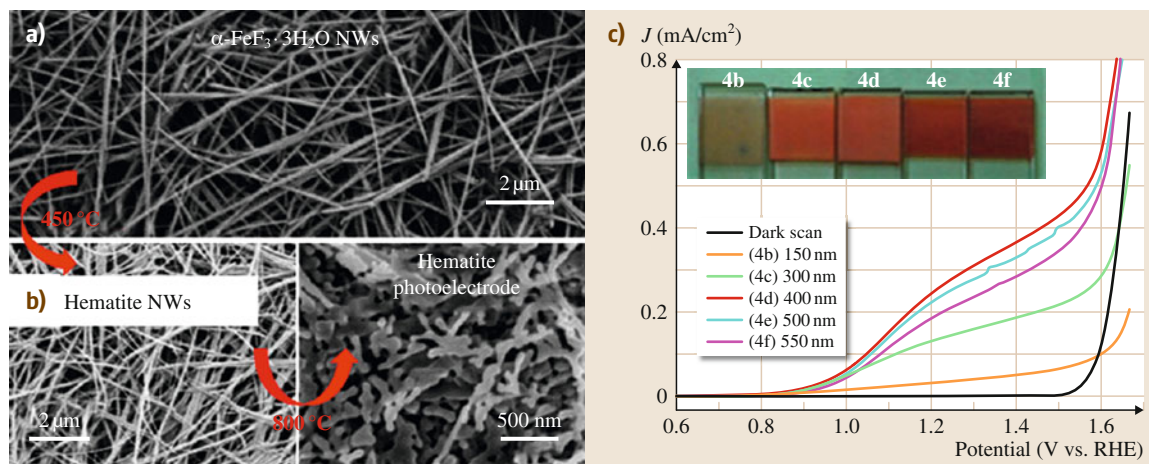
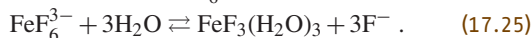


Fig. 17.27a,b Application of screw-dislocation-driven nanomaterials in solar energy conversion. SEM images of as-synthesized $\alpha\text{-FeF}_3 \cdot 3\text{H}_2\text{O}$ NWs (a) and converted hematite NW photoelectrode (b); photocurrent densities J versus bias voltage (V versus RHE) under AM1.5G simulated solar light at $100\text{ mW}/\text{cm}^2$ for hematite NW photoelectrodes of various thicknesses (after [17.16])

to favor NW growth. The following two reactions are responsible for NW growth:



The H_2O in the second equation comes from the hydrated Fe(III) salt and HF solution. F^- and H_2O should be considered as both reactants and ligands to the Fe^{3+} ions. This equilibrium likely helps maintain a constant and low supersaturation of $\text{FeF}_3(\text{H}_2\text{O})_3$, which is considered to be the precursor of crystal

growth for $\alpha\text{-FeF}_3 \cdot 3\text{H}_2\text{O}$ [17.99, 100]. The growth of $\alpha\text{-FeF}_3 \cdot 3\text{H}_2\text{O}$ NWs is likely driven by screw dislocations given the low supersaturation conditions applied in the synthesis [17.18–20], but the as-grown NW samples are not electron-beam stable due to the easy loss of lattice water, and thus it is impossible to either confirm or disprove this hypothesis. These $\alpha\text{-FeF}_3 \cdot 3\text{H}_2\text{O}$ NWs can be readily converted to semiconducting $\alpha\text{-Fe}_2\text{O}_3$ (hematite) NWs (Fig. 17.27b), which exhibited respectable PEC performance of $0.54\text{ mA}/\text{cm}^2$ photocurrent density at 1.23 V versus reversible hydrogen electrode potential (Fig. 17.27c).

17.7 Summary and Perspectives

This chapter has illustrated that the screw-dislocation-driven growth mechanism is applicable to many nanomaterials grown in solution or vapor phase, with the families of materials involved ranging from oxides and hydroxides, nitrides, chalcogenides, to metals. As the understanding of dislocation-driven growth deepens, this list of examples will continue to expand in the future. The procedures for microstructural characterization and confirmation of dislocation-driven growth discussed above can guide future work on searching for dislocation-driven growth. Moreover, the dislocation mechanism and elasticity theory could be used to explain other intriguing crystal growth phenomena that

are commonly observed but often unconvincingly explained.

Fundamental studies on dislocation-driven nanomaterial growth not only enhance the understanding of anisotropic crystal growth but also open up the exploitation of large-scale, low-cost solution growth for rational catalyst-free synthesis of anisotropic nanomaterials for diverse applications, such as those for renewable energy. The discussion in Sect. 17.5 established a general framework for rational design of dislocation-driven growth of nanomaterials.

It can also be expected that by utilizing dislocations one can fabricate more complex structures, such as het-

erojunctions with abrupt crystal interface, which could be of more interest than simple NWs/NTs for many applications, including solar energy conversion [17.101]. Engineering the locations and density of dislocations in substrates can enable control over the location and morphology of dislocation-driven NWs. Furthermore, it is interesting to investigate how a single axial screw

dislocation affects the physical properties of a single NW, including its electrical and mechanical properties. Deeper understanding of the screw-dislocation-driven growth of nanomaterials and their properties, and better control over such growth, will lead to a new stage of nanomaterial design and production for various applications.

References

- 17.1 M.J. Bierman, S. Jin: Potential applications of hierarchical branching nanowires in solar energy conversion, *Energy Environ. Sci.* **2**, 1050–1059 (2009)
- 17.2 J.R. Szczech, J.M. Higgins, S. Jin: Enhancement of the thermoelectric properties in nanoscale and nanostructured materials, *J. Mater. Chem.* **21**, 4037–4055 (2011)
- 17.3 Y. Xia, P. Yang, Y. Sun, Y. Wu, B. Mayers, B. Gates, Y. Yin, F. Kim, H. Yan: One-dimensional nanostructures: Synthesis, characterization, and applications, *Adv. Mater.* **15**, 353–389 (2003)
- 17.4 C.M. Lieber, Z.L. Wang: Functional nanowires, *MRS Bulletin* **32**, 99–108 (2007)
- 17.5 R.X. Yan, D. Gargas, P.D. Yang: Nanowire photonics, *Nat. Photonics* **3**, 569–576 (2009)
- 17.6 A.I. Hochbaum, P.D. Yang: Semiconductor nanowires for energy conversion, *Chem. Rev.* **110**, 527–546 (2010)
- 17.7 B. Tian, T.J. Kempa, C.M. Lieber: Single nanowire photovoltaics, *Chem. Soc. Rev.* **38**, 16–24 (2009)
- 17.8 X. Huang, S. Tang, X. Mu, Y. Dai, G. Chen, Z. Zhou, F. Ruan, Z. Yang, N. Zheng: Freestanding palladium nanosheets with plasmonic and catalytic properties, *Nat. Nanotechnol.* **6**, 28–32 (2011)
- 17.9 D.S. Kong, W.H. Dang, J.J. Cha, H. Li, S. Meister, H.L. Peng, Z.F. Liu, Y. Cui: Few-layer nanoplates of Bi₂Se₃ and Bi₂Te₃ with highly tunable chemical potential, *Nano Lett.* **10**, 2245–2250 (2010)
- 17.10 R.S. Wagner, W.C. Ellis: Vapor-liquid-solid mechanism of single crystal growth, *Appl. Phys. Lett.* **4**, 89–90 (1964)
- 17.11 A.M. Morales, C.M. Lieber: A laser ablation method for the synthesis of crystalline semiconductor nanowires, *Science* **279**, 208–211 (1998)
- 17.12 T.J. Trentler, K.M. Hickman, S.C. Goel, A.M. Viano, P.C. Gibbons, W.E. Buhro: Solution-liquid-solid growth of crystalline III–V semiconductors – An analogy to vapor-liquid-solid growth, *Science* **270**, 1791–1794 (1995)
- 17.13 F.D. Wang, A.G. Dong, J.W. Sun, R. Tang, H. Yu, W.E. Buhro: Solution-liquid-solid growth of semiconductor nanowires, *Inorg. Chem.* **45**, 7511–7521 (2006)
- 17.14 A.I. Persson, M.W. Larsson, S. Stenstrom, B.J. Ohlsson, L. Samuelson, L.R. Wallenberg: Solid-phase diffusion mechanism for GaAs nanowire growth, *Nat. Mater.* **3**, 677–681 (2004)
- 17.15 H.J. Fan, P. Werner, M. Zacharias: Semiconductor nanowires: From self-organization to patterned growth, *Small* **2**, 700–717 (2006)
- 17.16 D.S. Li, M.H. Nielsen, J.R.I. Lee, C. Frandsen, J.F. Banfield, J.J. De Yoreo: Direction-specific interactions control crystal growth by oriented attachment, *Science* **336**, 1014–1018 (2012)
- 17.17 H.G. Liao, L.K. Cui, S. Whitelam, H.M. Zheng: Real-time imaging of Pt₃Fe nanorod growth in solution, *Science* **336**, 1011–1014 (2012)
- 17.18 M.J. Bierman, Y.K.A. Lau, A.V. Kvit, A.L. Schmitt, S. Jin: Dislocation-driven nanowire growth and Eshelby twist, *Science* **320**, 1060–1063 (2008)
- 17.19 S. Jin, M.J. Bierman, S.A. Morin: A new twist on nanowire formation: Screw-dislocation-driven growth of nanowires and nanotubes, *J. Phys. Chem. Lett.* **1**, 1472–1480 (2010)
- 17.20 S.A. Morin, M.J. Bierman, J. Tong, S. Jin: Mechanism and kinetics of spontaneous nanotube growth driven by screw dislocations, *Science* **328**, 476–480 (2010)
- 17.21 I.V. Markov: *Crystal Growth for Beginners: Fundamentals of Nucleation, Crystal Growth, and Epitaxy* (World Scientific, Singapore 1995)
- 17.22 S.H. Oh, M.F. Chisholm, Y. Kauffmann, W.D. Kaplan, W. Luo, M. Ruhle, C. Scheu: Oscillatory mass transport in vapor-liquid-solid growth of sapphire nanowires, *Science* **330**, 489–493 (2010)
- 17.23 S. Hofmann, R. Sharma, C.T. Wirth, F. Cervantes-Sodi, C. Ducati, T. Kasama, R.E. Dunin-Borkowski, J. Drucker, P. Bennett, J.J. Robertson: Ledge-flow-controlled catalyst interface dynamics during Si nanowire growth, *Nat. Mater.* **7**, 372–375 (2008)
- 17.24 W.K. Burton, N. Cabrera, C. Frank: The growth of crystals and the equilibrium structure of their surfaces, *Philos. Trans. R. Soc. A* **243**, 299–358 (1951)
- 17.25 F.C. Frank: The influence of dislocations on crystal growth, *Discuss. Faraday Soc.* **23**, 48–54 (1949)
- 17.26 J.R. Hirth, J. Lothe: *Theory of Dislocations* (McGraw-Hill, New York 1968)
- 17.27 F.R.N. Nabarro: *Theory of Crystal Dislocations* (Oxford Univ. Press, London 1967)
- 17.28 F.C. Frank: Crystal growth and dislocations, *Adv. Phys.* **1**, 91–109 (1952)

- 17.29 G.W. Sears: A mechanism of whisker growth, *Acta Metall.* **3**, 367–369 (1955)
- 17.30 G.W. Sears: A growth mechanism for mercury whiskers, *Acta Metall.* **3**, 361–366 (1955)
- 17.31 G.W. Sears: Mercury whiskers, *Acta Metall.* **1**, 457–459 (1953)
- 17.32 S.S. Brenner, G.W. Sears: Mechanism of whisker growth – III nature of growth sites, *Acta Metall.* **4**, 268–270 (1956)
- 17.33 W.W. Webb, R.D. Dragsdorf, W.D. Forgeng: Dislocations in whiskers, *Phys. Rev.* **108**, 498–499 (1957)
- 17.34 R.D. Dragsdorf, W.W. Webb: Detection of screw dislocations in α -alumina whiskers, *J. Appl. Phys.* **29**, 817–819 (1958)
- 17.35 S. Amelinckx: Decoration of dislocations in alkali halide whiskers, *J. Appl. Phys.* **29**, 1610–1611 (1958)
- 17.36 C.M. Drum: Axial imperfections in filamentary crystals of aluminum nitride. I, *J. Appl. Phys.* **36**, 816 (1965)
- 17.37 C.M. Drum: Twist and axial imperfections in filamentary crystals of aluminum nitride. II, *J. Appl. Phys.* **36**, 824–829 (1965)
- 17.38 D.R. Veblen, J.E. Post: A TEM study of fibrous cuprite (chalcotrichite): Microstructures and growth mechanisms, *Am. Miner.* **68**, 790–803 (1983)
- 17.39 Y.K.A. Lau, D.J. Chernak, M.J. Bierman, S. Jin: Formation of PbS nanowire pine trees driven by screw dislocations, *J. Am. Chem. Soc.* **131**, 16461–16471 (2009)
- 17.40 J. Zhu, H.L. Peng, A.F. Marshall, D.M. Barnett, W.D. Nix, Y. Cui: Formation of chiral branched nanowires by the Eshelby Twist, *Nat. Nanotechnol.* **3**, 477–481 (2008)
- 17.41 J.D. Eshelby: Screw dislocations in thin rods, *J. Appl. Phys.* **24**, 176–179 (1953)
- 17.42 G.W. Sears: Twist in lithium fluoride Whiskers, *J. Chem. Phys.* **31**, 53–54 (1959)
- 17.43 I. Nikiforov, D.B. Zhang, T. Dumitrica: Screw dislocations in (100) silicon nanowires: An objective molecular dynamics study, *J. Phys. Chem. Lett.* **2**, 2544–2548 (2011)
- 17.44 D.B. Zhang, T. Dumitrica, G. Seifert: Helical nanotube structures of MoS_2 with intrinsic twisting: An objective molecular dynamics study, *Phys. Rev. Lett.* **104**, 065502 (2010)
- 17.45 F.C. Frank: Capillary equilibria of dislocated crystals, *Acta Crystallogr.* **4**, 497–501 (1951)
- 17.46 J. Heindl, H.P. Strunk, V.D. Heydemann, G. Pensl: Micropipes: Hollow tubes in silicon carbide, *Phys. Status Solidi (a)* **162**, 251–262 (1997)
- 17.47 S.A. Morin, S. Jin: Screw dislocation-driven epitaxial solution growth of ZnO nanowires seeded by dislocations in GaN substrates, *Nano Lett.* **10**, 3459–3463 (2010)
- 17.48 S. Hacialioglu, F. Meng, S. Jin: Facile and mild solution synthesis of Cu_2O nanowires and nanotubes driven by screw dislocations, *Chem. Commun.* **48**, 1174–1176 (2012)
- 17.49 T.B. Bateman: Elastic moduli of single-crystal zinc oxide, *J. Appl. Phys.* **33**, 3309–3312 (1962)
- 17.50 S.A. Morin, A. Forticaux, M.J. Bierman, S. Jin: Screw dislocation-driven growth of two-dimensional nanoplates, *Nano Lett.* **11**, 4449–4455 (2011)
- 17.51 H.H. Teng, P.M. Dove, J.J. De Yoreo: Kinetics of calcite growth: Surface processes and relationships to macroscopic rate laws, *Geochim. Cosmochim. Acta* **64**, 2255–2266 (2000)
- 17.52 H.H. Teng, P.M. Dove, C.A. Orme, J.J. De Yoreo: Thermodynamics of calcite growth: Baseline for understanding biomineral formation, *Science* **282**, 724–727 (1998)
- 17.53 I.V. Markov: *Crystal Growth for Beginners: Fundamentals of Nucleation, Crystal Growth, and Epitaxy* (World Scientific, Singapore 1995) p. 422
- 17.54 D.B. Williams, C.B. Carter: *Transmission Electron Microscopy* (Plenum, New York 1996)
- 17.55 A. Foitzik, W. Skrotzki, P. Haasen: Dislocation microstructure on (100) and (110) slip planes in lead sulphide, *Phys. Status Solidi (a)* **121**, 81–94 (1990)
- 17.56 E. Bauser, H. Strunk: Analysis of dislocations creating mono-molecular growth steps, *J. Cryst. Growth* **51**, 362–366 (1981)
- 17.57 H.Y. Wu, F. Meng, L.S. Li, S. Jin, G.F. Zheng: Dislocation-driven CdS and CdSe nanowire growth, *ACS Nano* **6**, 4461–4468 (2012)
- 17.58 F. Meng, S.A. Morin, S. Jin: Rational solution growth of α - FeOOH nanowires driven by screw dislocations and their conversion to α - Fe_2O_3 nanowires, *J. Am. Chem. Soc.* **133**, 8408–8411 (2011)
- 17.59 Y. Li, Y. Wu: Critical role of screw dislocation in the growth of Co(OH)_2 nanowires as intermediates for Co_3O_4 nanowire growth, *Chem. Mater.* **22**, 5537–5542 (2010)
- 17.60 F. Meng, S. Jin: The solution growth of copper nanowires and nanotubes is driven by screw dislocations, *Nano Lett.* **12**, 234–239 (2012)
- 17.61 L.H.G. Tizei, A.J. Craven, L.F. Zagonel, M. Tencé, O. Stéphan, T. Chiamonte, M.A. Cotta, D. Ugarte: Enhanced eshelby twist on thin wurtzite InP nanowires and measurement of local crystal rotation, *Phys. Rev. Lett.* **107**, 195503 (2011)
- 17.62 B. Aleman, Y. Ortega, J.A. Garcia, P. Fernandez, J. Piqueras: Fe solubility, growth mechanism, and luminescence of Fe doped ZnO nanowires and nanorods grown by evaporation–deposition, *J. Appl. Phys.* **110**, 014317 (2011)
- 17.63 Y.K. Ryu, P. Fernandez, J. Piqueras: Growth and characterization of Er-doped ZnO elongated nanostructures, *Phys. Status Solidi (a)* **208**, 868–873 (2011)
- 17.64 B.W. Jacobs, M.A. Crimp, K. McElroy, V.M. Ayres: Nanopipes in gallium nitride nanowires and rods, *Nano Lett.* **8**, 4353–4358 (2008)

- 17.65 Q. Wu, Z. Hu, X.Z. Wang, Y.N. Lu, X. Chen, H. Xu, Y. Chen: Synthesis and characterization of faceted hexagonal aluminum nitride nanotubes, *J. Am. Chem. Soc.* **125**, 10176–10177 (2003)
- 17.66 D. Maestre, D. Haeussler, A. Cremades, W. Jaeger, J. Piqueras: Nanopipes in In_2O_3 nanorods grown by a thermal treatment, *Cryst. Growth Des.* **11**, 1117–1121 (2011)
- 17.67 J. Bartolome, D. Maestre, M. Amati, A. Cremades, J. Piqueras: Indium zinc oxide pyramids with pinholes and nanopipes, *J. Phys. Chem. C* **115**, 8354–8360 (2011)
- 17.68 D. Maestre, D. Haussler, A. Cremades, W. Jager, J. Piqueras: Complex defect structure in the core of Sn-doped In_2O_3 nanorods and its relationship with a dislocation-driven growth mechanism, *J. Phys. Chem. C* **115**, 18083–18087 (2011)
- 17.69 J. Chikawa, T. Nakayama: Dislocation structure and growth mechanism of cadmium sulfide crystals, *J. Appl. Phys.* **35**, 2493–2501 (1964)
- 17.70 B.M. Bulakh: The real conditions of CdS single crystal growth from the vapour phase, *J. Cryst. Growth* **5**, 243–250 (1969)
- 17.71 G.H. Dierssen, T. Gabor: Growth mechanism of CdS platelets, *J. Cryst. Growth* **16**, 99–109 (1972)
- 17.72 C. Ma, Y. Ding, D. Moore, X.D. Wang, Z.L. Wang: Single-crystal CdSe nanosaws, *J. Am. Chem. Soc.* **126**, 708–709 (2004)
- 17.73 J.P. Ge, Y.D. Li: Selective atmospheric pressure chemical vapor deposition route to CdS arrays, nanowires, and nanocombs, *Adv. Funct. Mater.* **14**, 157–162 (2004)
- 17.74 J. Zheng, X.B. Song, N. Chen, X.G. Li: Highly symmetrical CdS tetrahedral nanocrystals prepared by low-temperature chemical vapor deposition using polysulfide as the sulfur source, *Cryst. Growth Des.* **8**, 1760–1765 (2008)
- 17.75 D. Cherns, L. Meshi, I. Griffiths, S. Khongphet-sak, S.V. Novikov, N.R.S. Farley, R.P. Champion, C.T. Foxon: Defect-controlled growth of GaN nanorods on (0001) sapphire by molecular beam epitaxy, *Appl. Phys. Lett.* **93**, 111911 (2008)
- 17.76 A. Navrotsky, L. Mazeina, J. Majzlan: Size-driven structural and thermodynamic complexity in iron oxides, *Science* **319**, 1635–1638 (2008)
- 17.77 N. Beermann, L. Vayssieres, S.E. Lindquist, A. Hagfeldt: Photoelectrochemical studies of oriented nanorod thin films of hematite, *J. Electrochem. Soc.* **147**, 2456–2461 (2000)
- 17.78 B. Tang, G.L. Wang, L.H. Zhuo, J.C. Ge, L.J. Cui: Facile route to α - FeOOH and α - Fe_2O_3 nanorods and magnetic property of α - Fe_2O_3 nanorods, *Inorg. Chem.* **45**, 5196–5200 (2006)
- 17.79 A. Saric, S. Music, K. Nomura, S. Popovic: Microstructural properties of Fe-oxide powders obtained by precipitation from FeCl_3 solutions, *Mater. Sci. Eng. B* **56**, 43–52 (1998)
- 17.80 M. Ozaki, S. Kratochvil, E. Matijevic: Formation of monodispersed spindle-type hematite particles, *J. Colloid Interface Sci.* **102**, 146–151 (1984)
- 17.81 K. Govender, D.S. Boyle, P.B. Kenway, P. O'Brien: Understanding the factors that govern the deposition and morphology of thin films of ZnO from aqueous solution, *J. Mater. Chem.* **14**, 2575–2591 (2004)
- 17.82 S.A. Morin, F.F. Amos, S. Jin: Biomimetic assembly of zinc oxide nanorods onto flexible polymers, *J. Am. Chem. Soc.* **129**, 13776–13777 (2007)
- 17.83 F. Wang, J.H. Seo, Z.Q. Ma, X.D. Wang: Substrate-free self-assembly approach toward large-area nanomembranes, *ACS Nano* **6**, 2602–2609 (2012)
- 17.84 H. Jiang, T. Zhao, C.Z. Li, J. Ma: Hierarchical self-assembly of ultrathin nickel hydroxide nanoflakes for high-performance supercapacitors, *J. Mater. Chem.* **21**, 3818–3823 (2011)
- 17.85 E. Suito, N. Uyeda: Electron microscopy and diffraction studies on the growth and structure of laminar single crystals of colloidal gold (Special Issue on Electron Microscopy), *Bull. Inst. Chem. Res. Kyoto Univ.* **42**, 511–541 (1965)
- 17.86 R.L. Penn, J.F. Banfield: Imperfect oriented attachment: Dislocation generation in defect-free nanocrystals, *Science* **281**, 969–971 (1998)
- 17.87 J. Baxter, Z. Bian, G. Chen, D. Danielson, M.S. Dresselhaus, A.G. Fedorov, T.S. Fisher, C.W. Jones, E. Maginn, U. Kortshagen, A. Manthiram, A. Nozik, D.R. Rolison, T. Sands, L. Shi, D. Sholl, Y. Wu: Nanoscale design to enable the revolution in renewable energy, *Energy Environ. Sci.* **2**, 559–588 (2009)
- 17.88 A.J. Nozik: Nanoscience and nanostructures for photovoltaics and solar fuels, *Nano Lett.* **10**, 2735–2741 (2010)
- 17.89 K. Sivula, F. Le Formal, M. Grätzel: Solar water splitting: Progress using hematite (α - Fe_2O_3) photoelectrodes, *Chem. Sus. Chem.* **4**, 432–449 (2011)
- 17.90 J.R. Szczech, S. Jin: Nanostructured silicon for high capacity lithium battery anodes, *Energy Environ. Sci.* **4**, 56–72 (2011)
- 17.91 Y. Lin, G. Yuan, S. Sheehan, S. Zhou, D. Wang: Hematite-based solar water splitting: Challenges and opportunities, *Energy Environ. Sci.* **4**, 4862–4869 (2011)
- 17.92 A. Ennaoui, S. Fiechter, C. Pettenkofer, N. Alonso-Vante, K. Büker, M. Bronold, C. Höpfner, H. Tributsch: Iron disulfide for solar energy conversion, *Sol. Energy Mater. Sol. Cells* **29**, 289–370 (1993)
- 17.93 M. Caban-Acevedo, M.S. Faber, Y.Z. Tan, R.J. Hamers, S. Jin: Synthesis and properties of semiconducting iron pyrite (FeS_2) nanowires, *Nano Lett.* **12**, 1977–1982 (2012)
- 17.94 F. Badway, N. Pereira, F. Cosandey, G.G. Amatucci: Carbon-metal fluoride nanocomposites. Structure and electrochemistry of $\text{FeF}_3\text{:C}$, *J. Electrochem. Soc.* **150**, A1209–A1218 (2003)

- 17.95 L.S. Li, Y.H. Yu, F. Meng, Y.Z. Tan, R.J. Hamers, S. Jin: Facile solution synthesis of α -FeF₃·3H₂O nanowires and their conversion to α -Fe₂O₃ nanowires for photoelectrochemical application, *Nano Lett.* **12**, 724–731 (2012)
- 17.96 C. Wadia, A.P. Alivisatos, D.M. Kammen: Materials availability expands the opportunity for large-scale photovoltaics deployment, *Environ. Sci. Technol.* **43**, 2072–2077 (2009)
- 17.97 W.M. Haynes: Physical constants of inorganic compounds. In: *Handbook of Chemistry and Physics*, Vol. 91, ed. by D.R. Lide (CRC, Boca Raton 2010)
- 17.98 R.K. Hocking, S. DeBeer George, K.N. Raymond, K.O. Hodgson, B. Hedman, E.I. Solomon: Fe L-Edge X-ray absorption spectroscopy determination of differential orbital covalency of siderophore model compounds: Electronic structure contributions to high stability constants, *J. Am. Chem. Soc.* **132**, 4006–4015 (2010)
- 17.99 K.M. Forsberg, A.C. Rasmuson: Crystallization of metal fluoride hydrates from mixed hydrofluoric and nitric acid solutions, Part I, Iron (III) and Chromium (III), *J. Cryst. Growth* **312**, 2351–2357 (2010)
- 17.100 K.M. Forsberg, A.C. Rasmuson: Crystal growth kinetics of iron fluoride trihydrate, *J. Cryst. Growth* **296**, 213–220 (2006)
- 17.101 G. Dhanaraj, K. Byrappa, V. Prasad, M. Dudley (Eds.): *Springer Handbook of Crystal Growth* (Springer, Berlin, Heidelberg 2010)